2008

Health Monitoring of Cracked Rotor Systems Using External Excitation Techniques

Adam C. Wróblewski
Cleveland State University

HEALTH MONITORING OF CRACKED ROTOR SYSTEMS USING EXTERNAL EXCITATION TECHNIQUES

ADAM C. WRÓBLEWSKI

Bachelor of Science in Mechanical Engineering

Cleveland State University

December, 2006

Submitted in partial fulfillment of requirements for the degree

MASTER OF SCIENCE IN MECHANICAL ENGINEERING

At the

CLEVELAND STATE UNIVERSITY

December, 2008

This thesis has been approved

For the Department of Mechanical Engineering

And the College of Graduate Studies by

Dr. Jerzy Sawicki

Department/Date

Dr. John Frater

Department/Date

Dr. Ana Stankovic

Department/Date

ACKNOWLEDGEMENTS

I would like to thank Dr. Jerzy T. Sawicki for his exceptional work acting as my advisor. His dedication to this field of research is what motivated me to put forth the effort required to successfully complete my Master's degree at Cleveland State University. His insights and technical understanding of rotordynamics kept me focused on many tasks during this work.

I would like to thank Dr. Frater and Dr. Stankovic for being committee members as well as reviewing my thesis and attending my thesis presentation. They have made helpful suggestions in improving and strengthening my work. I would like to thank a classmate of mine, Alex Pesch, who has aided me with various tasks. Many thanks to Dave Epperly who has done an extraordinary job in support of the rotor test rig. I would also like to thank Dr. Mark Wernet (NASA) and Dr. Randy Locke (ASRC) for providing me a flexible work schedule in order to accommodate class time and thesis work.

Finally, I would like to thank my parents, Michael and Maria, for fully supporting me throughout my education. Their continuous encouragement has provided me with the motivation required to complete a graduate degree.

HEALTH MONITORING OF CRACKED ROTOR SYSTEMS USING EXTERNAL EXCITATION TECHNIQUES

ADAM C. WROBLEWSKI

ABSTRACT

Cracked rotors present a significant safety and loss hazard in nearly every application of modern turbomachinery. This thesis focuses on the health monitoring, modeling, and analysis of machines with transverse breathing cracks, which open and close due to the self-weight of the rotor. After considering the modeling of cracked rotors, the thesis investigates an active structural health monitoring approach, focusing on the application of an active magnetic actuator to apply a specially designed external force excitation to the rotating shaft. Extensive experimental data has been collected and analyzed utilizing advanced diagnostic techniques. The presented results demonstrate that the use of a magnetic force actuator to apply external excitation has potential in the diagnostics of cracked rotors. The observed unique crack signatures demonstrate the ability of the method for early diagnosis of transverse rotor cracks.

TABLE OF CONTENTS

LIST OF FIGURES

LIST OF TABLES

NOMENCLATURE

α = Ball bearing contact angle, degrees

C = Magnetic bearing calibration factor

D = Ball diameter in ball bearing, mm

$\mathbf{D}$ = Damping matrix

E = Modulus of elasticity, GPa

F_{AMB} = AMB magnetic force, N

$F_{Bearing}$ = Ball bearing radial load, N

$\mathbf{G}$ = Gyroscopic matrix

G = Shear modulus, GPa

g = Gravitational constant, 9.81 m/s^2

g_{AMB} = Effective gap, mm

θ = Angle between crack axis and rotor response, radians

θ_0 = Initial angle between crack axis and rotor response, radians

θ_1 = Angle between crack axis and rotor response plus initial angle, radians

I = Number of active rows in ball bearing

I_{top} = Measured current of top quadrant of AMB, Amp

I_{bottom} = Measured current of bottom quadrant of AMB, Amp

$\mathbf{K}_0$ = Un-cracked stiffness matrix in non-rotating coordinates

$\mathbf{K}_c$ = Stiffness reduction matrix in non-rotating coordinates

$\tilde{\mathbf{K}}_0$ = Un-cracked stiffness matrix in rotating coordinates

$\tilde{\mathbf{K}}_c$ = Stiffness reduction matrix in rotating coordinates

$\tilde{\mathbf{K}}_{cr}$ = Stiffness of cracked rotor in rotating coordinates

$\tilde{\mathbf{K}}_1$ = Stiffness matrix when crack is open in rotating coordinates

K_R = Ball bearing stiffness, MN/m

$\mathbf{M}$ = Mass matrix

n = Integer value for application in combination frequency equation

ρ = Material density, kg/m^3

$\mathbf{Q}_{AMB}$ = AMB force vector

$\mathbf{Q}_u$ = Unbalance force vector

q = Shaft total deflection, m

q_{st} = Shaft static deflection, m

q_{dy} = Shaft dynamic deflection, m

t = Time, s

$\mathbf{T}$ = Coordinate transformation matrix

υ = Poisson's ratio

$\mathbf{W}$ = Gravitational force matrix

ω_n = Rotor critical speed, rad/s or Hz

Ω = Rotational speed, rpm or Hz

Ω_{AMB} = Combination frequency to apply to the rotating shaft via AMB, rad/s or Hz

x_{AMB} = Actual displacement of shaft relative to stator, mm

Z = Number of active balls in ball bearing

CHAPTER I

INTRODUCTION

1.1 Background and Motivation

The term *structural health monitoring* can be described as the practice of implementing a method that continuously diagnoses the integrity of a structure. This method involves the observation of a structure over time and the recognition of key features in the measurements. Measurements taken during a state in which the system is known to be un-cracked can be thought of as the healthy system's *proper operational envelope*. This *proper operational envelope* is recorded and stored for continuous comparison with current measurements in order to detect any trends exceeding the normal operational range. Discrepancies between the healthy system's history and the current measurements indicate changes in the structure. By knowing the magnitude and the rate of change, appropriate steps can be taken prior to failure of the system.

Many applications of turbomachinery such as gas turbines, compressors or pumps are pushed to run past their expected lifespan which leads to progressive structural fatigue, and consequently, to catastrophic failure. The ability to monitor the structural health of a system is extremely important in maintaining safe machine operation and reducing the risk of unexpected shutdown.

1.2 Objective of Thesis

The objective of this thesis is to utilize a rotor test rig equipped with both active magnetic bearings (AMBs) and conventional ball bearings to investigate the effects of a transverse surface crack on a shaft. Specifically, this thesis investigates the rotor's dynamic response due to effects from a breathing crack which opens and closes due to the self-weight of the rotor.

The rotor in the tested configuration is supported by conventional ball bearings. The AMB is only used as an actuator to apply a force input directly to the rotor in order to induce additional frequencies in the system's response. Employing the rotor test rig shows that a breathing crack in a shaft can be detected by means of applying a specified harmonic force via an AMB actuator while being supported on the commonly used rolling element bearings. The approach of introducing AMBs for health monitoring for non-magnetically levitated rotors allows for a much broader spectrum of applications.

Chapter 2 reviews common faults seen in rotating machinery and illustrates FFT spectrums which can aid in diagnosis. Monitoring and excitation hardware is described in order to justify the hardware used in the test rig for this research. A literature review

examines others' works that have contributed to the field of rotor health monitoring and specifically to the subject of this thesis.

Chapter 3 describes in detail the modeling of a rotor with a transverse surface crack. This modeling specifically focuses efforts to model the breathing crack which is caused by rotation and the self weight of the rotor. To illustrate the effectiveness of the finite element modeling technique, an idealized rotor is modeled and the results are provided.

As a precursor to the experimental data, Chapter 4 contains a detailed description of the test rig used in this work as well as a figure which illustrates how all the major components work together. Noteworthy components, such as the AMB actuator and the shafts with Electrical Discharge Machining (EDM) cuts, are presented here in detail. In addition, the data acquisition and signal injection systems are reviewed.

Chapter 5 contains the FFT results described in detail, as well as system identification results. Following the identification of the rotor's natural frequencies, experimental data is plotted for the various conditions which include a combination of various harmonic injection signals coupled with various shaft crack configurations. Once experimental data is presented, it is compared to simulated data from the finite element modeling.

Finally, Chapter 6 presents the conclusions of the thesis.

CHAPTER II

STATE-OF-THE-ART OF ROTOR HEALTH MONITORING

2.1 Introduction

Rotating machinery has been becoming faster and more lightweight due to exceptional amounts of progress in engineering and materials. In addition, rotating machines have been required to have much longer life spans which makes detection and analysis of faults increasingly important in avoiding failures.

Making use of vibration analysis, the condition of a machine can be continuously monitored. Detailed analysis can even identify unique responses in the measurements which can be directly linked to particular faults. Correlations of vibration responses to specific machinery faults have long been established and will be reviewed in Section 2.3.

The most important factors that an operator monitors are the amplitudes and phase of vibrations and how they are trending. Generally, this information is all the operator gets in order to make proper operational decisions. However, this is not a trivial task. Even the healthiest rotating machines exhibit changes in amplitude and phase during normal operation which are of acceptable vibration levels. These minute changes can be associated to a wide variety of factors that, most likely, operators have little or no control over. These changes are normal effects from factors that can include load changes, thermal transitions, normal wear, and fluctuations in the machine's environment. In the case where vibrations begin to grow and fall out of the established normal operational envelope, the operator needs to track the trends carefully and ascertain the most appropriate course of action for the particular situation. In such situations, there can be a few different courses of action, such as a temporary change in operating condition to bring the machine back to acceptable vibration levels, or plan an early shut-down of the machine to perform maintenance, or an immediate shutdown when vibration levels grow rapidly.

The primary tool an operator has in diagnosing vibration amplitude and frequency content is the Fast Fourier Transform (FFT). This tool is used to analyze vibration signals from sensors placed in appropriate locations along the machine and decompose them into the various frequencies that it contains. This will be briefly discussed in the following section.

2.2 Fast Fourier Transform (FFT)

Vibration signals collected from rotating machinery are often very complex which makes them very difficult to interpret in the time domain. In order to analyze them, it is necessary to transform them from the time domain into the frequency domain. In the early 1800's, a French mathematician named Joseph Fourier proved that all waveforms are composed of many individual frequencies which can be broken down into their separate components mathematically [**1**]. This concept is based on the Fourier Integral. However, this mathematical technique was not used extensively until the development of computers due to its computationally intensive nature. Today, this technique is in the curriculum of every engineering program [**2**].

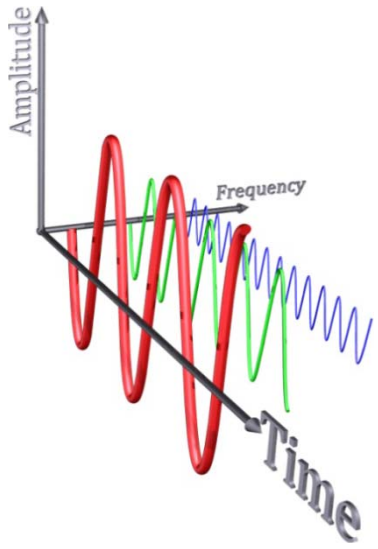

Figure 1 FFT concept, amplitude vs. time and frequency.

Figure 1 illustrates the concept of the FFT where both the time and frequency axis are plotted against amplitude. If one looks normal to the time axis (time domain), the

complex signal of many frequencies added together can be seen which can be extremely difficult to interpret. If one looks normal to the frequency axis (frequency domain), only amplitudes of particular frequencies that the raw signal contains are seen which are much more practical for diagnostic purposes. This tool is extremely useful for determining what dominant frequencies are present in a particular vibration signal and will be extensively used throughout this work.

Of course, FFT is not limited to rotary vibrations. This tool can be applied to almost any field of physical science that uses sinusoidal signals, such as engineering physics, chemistry, and applied mathematics. In addition, FFT digital signal processing is very common for applications in communications, astronomy, optics, and even geology.

2.3 Overview of Rotor Malfunctions

Some of the possible machinery defects that can be detected using vibration analysis include unbalance, bent shaft, eccentricity, misalignment, looseness, gear defects, bearing defects, oil whirl, cavitations, shaft cracks, and rotor rubs. The ability to identify these faults plays an important role in the mission for longer lasting and more reliable machines which is why it is important to know how to identify key features in the frequency spectrum (FFT) plot. The vibrations of a rotor will exhibit characteristic features based on what type of defect is present, which allows an operator to deduce a probable cause. It is common to annotate frequencies that are multiples of the rotation speed as 1X, 2X, 3X, and so on, while other non-multiple frequencies can be denoted

explicitly. Using these types of annotations to describe FFT spectrums allows for identification of certain rotor malfunctions mentioned earlier. A few popular examples of rotor malfunctions are described below, including their description and characteristic FFT spectrums.

Unbalance of a rotor is probably the most common defect in rotating machinery. It is defined by the International Standards Organization (ISO) to be a condition which exists in a rotor when vibratory force or motion is imparted to its bearings as a result of centrifugal force. A conceptual depiction of planar mass unbalance on a shaft is shown in Figure 2, however, coupled unbalance is commonly seen as well which can be depicted as two unbalance masses that do not share a common plane. More often than not, unbalance is caused by less than perfect manufacturing, which include the use of materials with non-uniform density, holes that are not symmetrically drilled about the rotating axis, and other machining imperfections or even assembly errors. In addition, unbalance can accumulate over time during normal operation from factors such as uneven product depositions, damage, missing material, and even thermal distortions. As a result, every rotor will exhibit a predominant 1X (rotation speed) frequency in the spectrum plot which is generally considered normal. Figure 3 illustrates the dominant 1X component in the frequency spectrum plot which indicates that most of the vibratory response of this machine is at the same frequency as the rotational velocity. Since every machine will have some degree of unbalance, one must know the acceptable operating envelope for the 1X amplitude to determine if balancing is necessary.

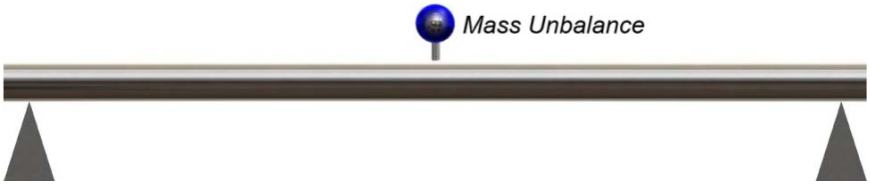

Figure 2 Conceptual drawing of mass unbalance.

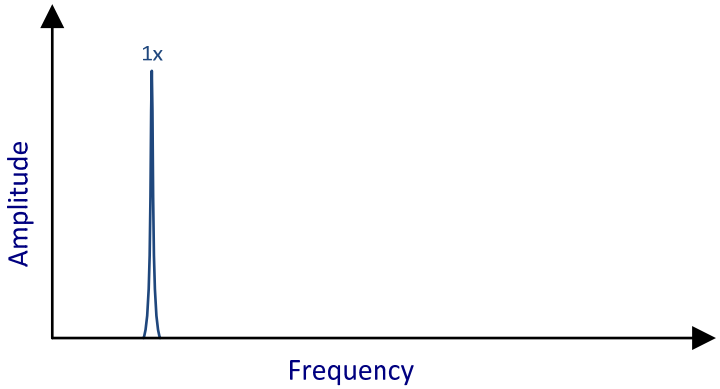

Figure 3 FFT spectrum indicative of pure unbalance.

There are well established balancing methods that employ various techniques but the concepts are generally synonymous. The radial location on the rotor where there is excessive radial mass is referred to as the heavy spot. This heavy spot can be augmented by adding mass in an exact opposite location relative to the axis of rotation. Unfortunately, it is difficult to find the location of a heavy spot; instead, the high spot is sought after, which is the radial location in the shaft's orbit where the displacement is the greatest. It should be noted that balancing for one speed range may not always apply to another speed range. This is because of a phase relationship between the heavy spot and high spot. The heavy spot and high spot are in the same location for rotors that run below

their critical speeds. However, as the rotor approaches resonance, the phase shifts 180˚ as critical speed is passed. As the rotor continues to increase its rotational speed and pass through another critical speed, there will be another phase shift of 180˚ which relocates the high spot to be near the heavy spot as they originally started. This relationship continues as subsequent critical speeds are passed. Balancing techniques rely on measuring phase to locate the high spot, ascertaining the relationship between the high spot and the heavy spot, and determining the unbalance through the use of correction weights [**3**].

Bent shafts are generally caused by a damaging event, imperfect manufacturing, or even thermal distortions. A shaft without a relatively straight geometry will have both 1X components and 2X components in the FFT spectrum as well as high vibration amplitudes in the radial and axial directions. However, the dominant frequency component is dependent on the location of the bend on the shaft. If the bend is near the shaft center, the 1X component amplitude will be dominant. If the bend is near the shaft end, the 2X component amplitude will be dominant [**4**]. For illustration purposes, Figure 4 shows a conceptual drawing of a bent shaft with the bend at the center. The FFT corresponding to this shaft is shown in Figure 5, where the 1X component is dominant relative to the 2X component.

Figure 4 Conceptual drawing of shaft bend at center.

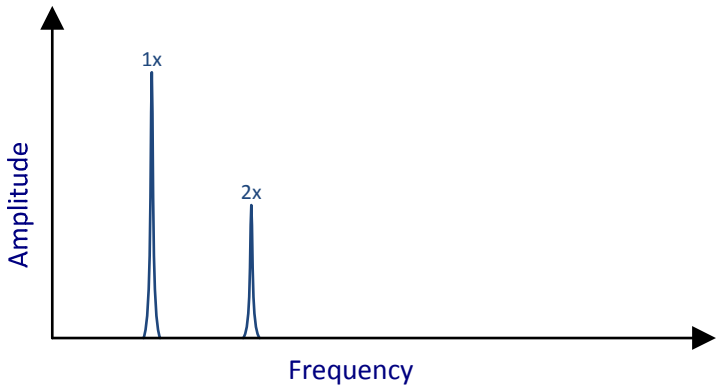

Figure 5 FFT spectrum indicative of a bent shaft.

Misalignment is considered to be the second most common defect in rotating machinery following unbalance. This fault can appear in the form of angular misalignment depicted in Figure 6 or parallel misalignment depicted in Figure 8, but most commonly will appear in combination with each other. Despite the importance of properly aligned rotors, literature on rotor misalignment is very scarce. Very little is published on the destructive, overloading effects on rotors and bearings, or on methods of diagnosing this defect using vibration monitoring [**5**].

Misalignment mainly causes the generation of rotor load in specific radial or angular directions. In the case of induced constant radial force, the rotor is pushed to one side in the corresponding direction and becomes displaced. In the case of constant angular force, the rotor may be forced to rotate in a bowed configuration.

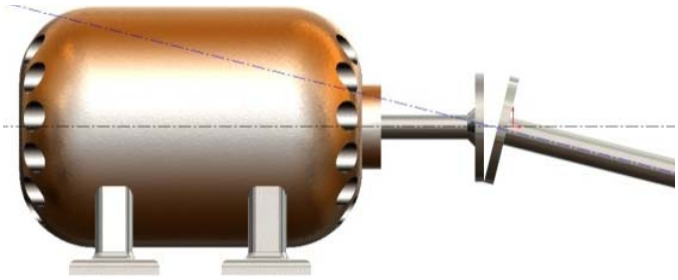

Figure 6 Conceptual drawing of angular misalignment.

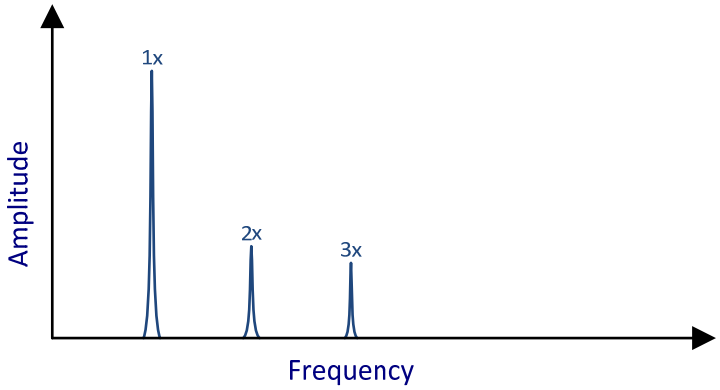

Figure 7 FFT spectrum indicative of angular misalignment.

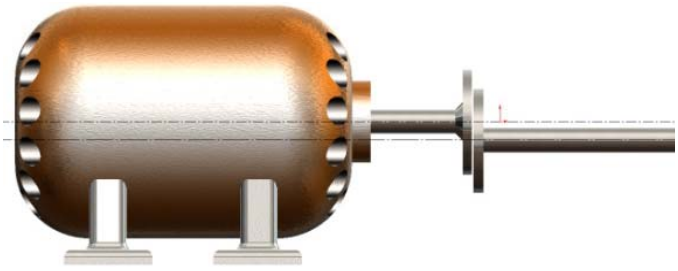

Figure 8 Conceptual drawing of parallel misalignment.

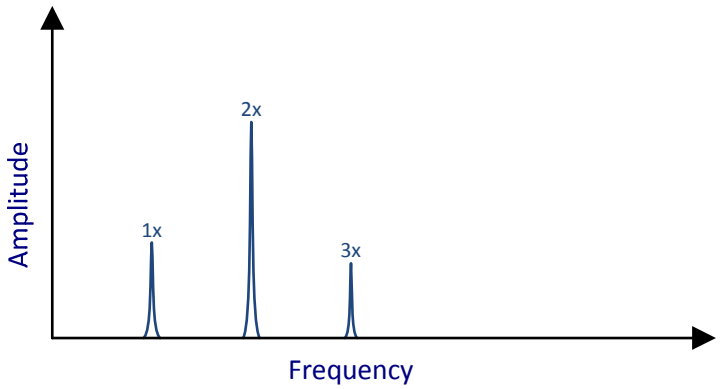

Figure 9 FFT spectrum indicative of parallel misalignment.

General FFT spectrums of misalignment are uncommon due to the obscurity in diagnosis of this fault [**6**]. The response of a rotor that is misaligned is heavily dependent on rotor speed, coupling type, coupling stiffness, and the magnitude of misalignment. However, FFT spectrums of possible indications of misalignment have been established by some authors and examples of these are shown. In the case of angular misalignment, the driver and the driven machine shafts are subjected to both axial and radial vibrations at a 1X frequency. Due to the rarity of pure angular misalignment, the FFT response will not have a pure 1X component. Typically, there will be high vibrations with both 1X and 2X components that are commonly accompanied by a 3X as shown in Figure 7 [**3**] [**4**]. In the case of mostly parallel misalignment, the FFT will show a high 2X component due to its 2 hits per cycle nature where the FFT is illustrated in Figure 9 [**3**] [**4**]. As stated before, it is rare to have purely parallel misalignment which will result in the FFT spectrum containing other frequencies in addition to the dominant 2X component.

Mechanically Loose Connections and Rubs can be categorized together for the resason that they exhibit similar behaviors. However, the priniciple difference between them is that mechanical looseness can be considered as momentary reduction in machine stiffness whereas a rub can be considered as a momentary increase in stiffness. Mechanically loose connections are generally found in bearing caps, bearing mounts, base mounts, or other hardware that constrains the rotational centerline to a fixed location. Similar behavior can be exhibited by looseness of rotating components directly mounted to the shaft such as gears, impellers, compressors, turbines, etc. On the other hand, rotor rub is always a secondary effect manifested by other faults that cause the rotating component to impact a stationary component, such as excessive radial loads, looseness, misalignment, uneven thermal growth, and a host of others. This contacting may be partial or continuous throughout the cycle. The dynamic characterististics created by mechanical loosenes and rotor rub will likely introduce a significant degree of nonlinearity in its behavior. One can expect to have intermittant hard contacting of components throughout the operational range which will yield a rich vibration spectrum with several prominant harmonics as well as integer subharmonics and their multiples [**2**]. In order to differentiate the measurements of mechanical loosness and rotor rub from other faults that contain similar frequencies, it is important to take measurements in different axial and radial locations on the machine. Mechanical loosness and rotor rub are often highly directional and are dictated by the specific direction and location of the fault [**4**]. A FFT plot indicative of mechanically loose components or rotor rub is shown in Figure 10.

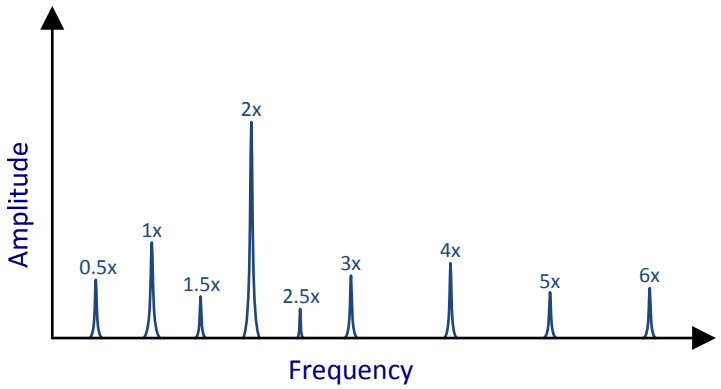

Figure 10 FFT spectrum indicative of mechanical looseness.

Oil Whirl is a fluid induced instability that is known to occur in fluid-pressure lubricated bearings also known as journal bearings. In journal bearings, the shaft or journal is designed to float on a thin film of fluid that is housed within the bearing. In order for this to work, the journal must rotate eccentrically relative to the bearing housing to produce converging surfaces where high fluid pressures are produced, upon which the journal is supported. Under known loading, a properly designed journal bearing only operates in a certain speed range requiring a specified fluid viscosity. In the case where the journal's rotational speed, or fluid viscosity is too low, or the rotor load is too great, the film that supports the rotor may become too thin allowing destructive contacts in the direction of the load between the journal and bearing. On the other hand, if the rotational speeds or fluid viscosities are too high or the rotor load is decreased, the supportive fluid pressures pushes the journal to the center of the bearing, eliminating the desired eccentricity, which will cause the journal to perform unpredictably within the bearing. This effect of unstable operation is referred to as oil whirl. Figure 11 illustrates the

journal eccentrically positioned within the bearing and also the destructive behavior of oil whirl.

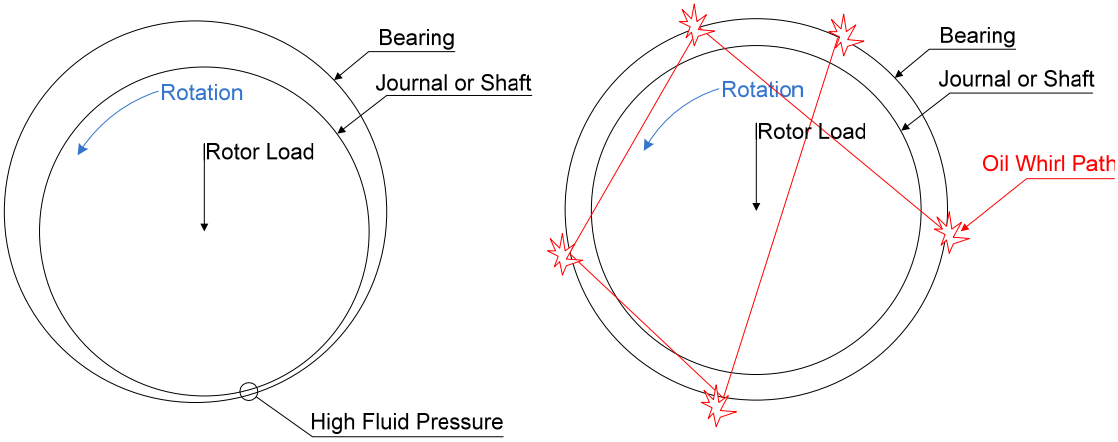

Figure 11 Left: Stable journal position. Right: Unstable journal position.

Generally, oil whirl occurs when the rotor passes through its critical speed. However, it can be controlled to some degree by maintaining proper rotational velocities, fluid viscosities, and rotor loads. Oil whirl frequency usually occurs at 0.42 to 0.48 times the shaft rotational speed and is often quite severe and considered excessive when displacement amplitudes exceed 50% of the bearing clearances [**1**]. In the FFT spectrum, the 1X component represents the rotation speed; however, the distinguishable frequency component would be a 0.42X to 0.48X as shown in Figure 12. The 1X component is shown because virtually every rotating system will exhibit this.

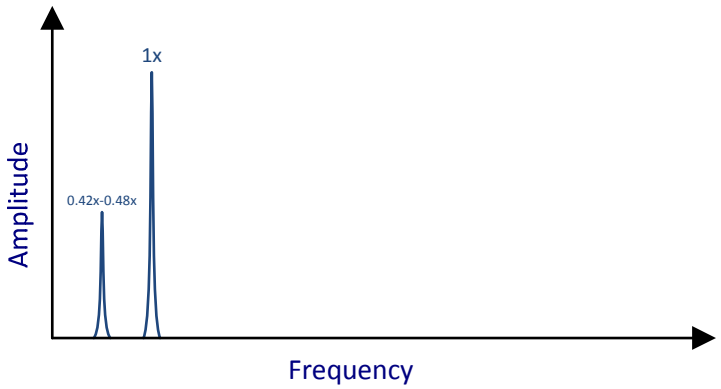

Figure 12 FFT Spectrum indicative of oil whirl.

2.4 Measurement and Excitation Hardware

The demand for performance, reliability, and safe operation of rotating machinery is always growing, which fuels a high demand for understanding and controlling the dynamics of a system. This demand drives technological advances in all areas of engineering which is crucial for the development of new concepts and ideas to achieve new levels of machine performance. In today's world, engineers are approaching the limit of what simple mechanical systems can achieve. With this in mind, it is necessary to continue integrating electronics and digital control systems which will allow for enhanced monitoring, understanding, and control of complex dynamics of rotating machinery.

2.4.1 Measurement Hardware in Rotating Machinery

In order to begin to understand the dynamics of rotating machinery, it is essential to have the ability to monitor extremely quick and minute movements of the rotor. This requires the employment of a method that is accurate, non-intrusive, and high speed. A non-intrusive method is imperative in order to take measurements without physical contact to the rotor in an effort to eliminate foreign disturbances to the normal operation of the machine. This ensures that there are no outside effects to the rotor's dynamics, as well as eliminating any additional sources of contact wear. The sensors must also be able to perform measurements accurately at high rates in order to properly capture the vibration patterns of a spinning rotor. Common sensors perform with frequency response rates near 10 kHz and can vary in operating distances from tens of microns to tens of millimeters.

Condition monitoring of rotating machinery is mostly subjected to the use of three types of sensors: accelerometers, keyphasors, and proximity probes. In this research, only proximity sensors and a keyphasor are used to collect vibration data, however, accelerometers deserve mention as well in this section.

Proximity Sensors detect distances of metal targets without any physical contact by emitting electromagnetic fields and monitoring the changes in them. Various types of probes are available to accomplish such a task like the variable reluctance sensor or the eddy current sensor. In this work, the eddy current probes will be utilized to monitor rotor performance.

Eddy current probes operate by radiating a high frequency RF signal (in the MHz range) from the probe tip which is generated by an oscillator/demodulator and transmitted via cable. Eddy currents are generated on the surface of the metal target which is then detected by the receiver coil. The received signal then provides a voltage which is directly proportional to the distance being measured. In addition, eddy current sensors are unaffected by water, oil, and other contaminants which make them ideal for many applications.

Keyphasors are sensors that are used for monitoring the phase or angular position of the rotor. This type of measurement is crucial for machine monitoring because it provides necessary phase information, which is necessary for understanding rotor dynamic behavior and is needed for a control system if applicable. There are many types of keyphasors but they can be categorized into two groups: voltage generating types and pulse generating types.

In the category of voltage generating keyphasors, there is DC generator keyphasors and drag cup keyphasors. They both operate similarly by producing more voltage the faster they turn. However, the DC generator produces DC voltage as the name implies and the drag cup produces AC voltage. In addition, these sensors can provide direction of rotation which can be useful in a variety of applications.

Pulse generating keyphasors work on the principle of counting pulses and relating them to time. Sine waves or pulses are outputted that are counted which require are more complicated digital circuit to complete the process of counting, storing, calculating, and finally displaying results. This can be done a vast array of keyphasors types such as

photocell keyphasors, toothed rotor keyphasors, capacitance keyphasors, and many others.

Accelerometers are devices for measuring accelerations by electromechanically producing voltages or charges that are proportional to the loads that they're subjected to. There are many ways to make an accelerometer work. One of the more popular ways is through the exploitation of a piezoelectric crystal's inherent properties to output voltages proportional to the accelerations it is subjected to. Another common way to create an accelerometer is by sensing changes in the capacitance of two microstructures that are placed next to each other. During accelerations, one of the microstructures will move slightly and create a change in the capacitance between them. Through the use of circuitry, capacitance can be converted to voltage and finally the voltage signal can be interpreted by a data acquisition system. Having the ability to measure acceleration, one can analyze the way a component is moving.

2.4.2 Excitation Hardware in Rotating Machinery

Excitation methods for the purpose of system identification in rotating machinery have long been an appealing topic of research. Experimental techniques for extracting dynamic properties of seals, bearings, and other shaft properties have been improving for years in attempts to design rotating machinery utilizing more accurate system parameters [**7**]. In addition, carefully designed external excitation techniques are being developed to enhance subtle vibration responses that may indicate machine faults. Many kinds of actuators are candidates for such purposes; however the use of the AMB will be

examined in this work. A few excitation techniques are discussed beginning with a brief history.

Oil film bearing coefficients for a fully operating turbomachine were first identified by Morton [**8**] in 1975 by an impact which is a simple broadband excitation technique. This impact was executed by employing a rig that preloaded a rotating shaft with a static force and then instantly releasing the load by breaking a link [**9**], where the impact force was measured with a strain gauge as shown in Figure 13.

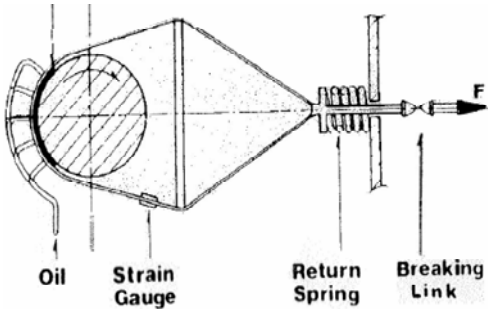

Figure 13 Morton's oil film coefficient test rig [8**].**

Nordmann and Schollhorn [**10**] and Tonnesen and Lund [**11**] excited a rotating Jeffcott rotor supported on oil film bearings by a hammer. The impact force and displacement signals were used for identification of the modal parameters of the rotating system. One of the disadvantages of the broadband excitation in general is the distribution of the energy over a certain frequency range, which may cause a poor signal to noise ratio. Iwatsubo *et al.* [**12**] used an external excitation technique to analyze the response of the cracked shaft. He showed the presence of combination harmonics due to interaction between impact force and rotation of shaft, and considered them as the crack indicators [**13**].

In order to make actuators practical, they should conform to some guidelines. For example, actuators should be:

- Compact as possible, space is generally quite limited.
- Lightweight, for aeronautical or space applications.
- Powerful, to produce large forces relative to the mass being moved.
- Responsive, in order to output the desired frequency range.

These as well as other factors need to be considered when choosing an actuator. Most commonly available types are piezoelectric actuators, hydraulic actuators, and magnetic actuators.

Piezo actuators have been commonly used for some time and are suitable for use in small movement applications, generally on the scale of μm. They are constructed of stacked piezoelectric crystal wafers in columns. Applying an electric field causes them to deform and produce small movement. The amount of total deformation is known as the regulating distance which is dependent on the number of crystal wafers in the stack. A schematic of a piezo actuator is shown in Figure 14. In order for this actuator to operate on a rotating shaft, it must be directly tied to some type of bearing that is coupled to the rotating shaft. Piezoelectric actuators are known for their high stiffness and their performance in high frequency ranges [**7**]. However, the fundamental disadvantage of the piezoelectric actuator is that its regulating distance is very small. This distance can be increased but will prescribe much larger actuator sizes.

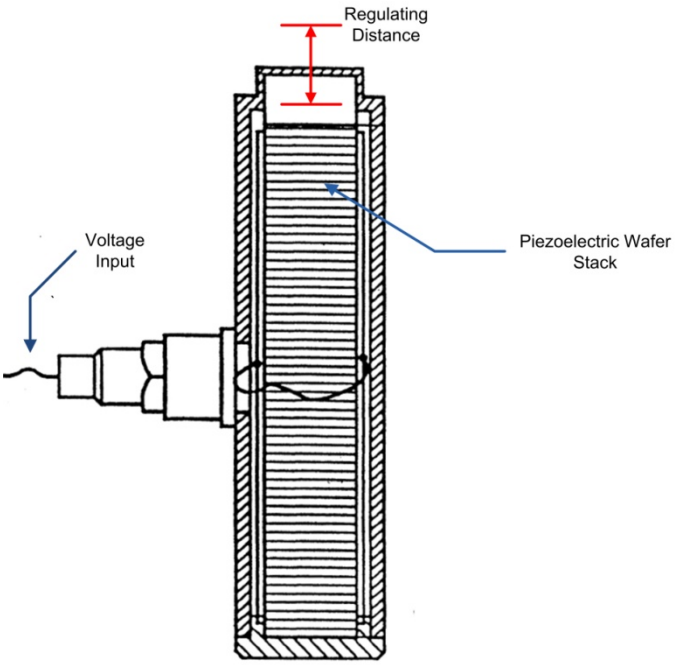

Figure 14 Schematic of a piezoelectric linear actuator [7].

A *hydraulic actuator* design described by Ulbrich [**7**] is shown in Figure 15. This actuator design consists of two cylindrical chambers which are closed in the working direction by elastic membranes. The pressure difference between the two chambers 1 and 2 is necessary to create the regulating operation which is supplied by the servo valve. The actuating force to the rotating shaft is then transmitted via a bearing which connects the actuator to the shaft. The special design of the actuator yields a high radial stiffness and ensures a corresponding safety against tilting effects (depending on the distance between the two membranes as well as on their thickness). When using these actuators to control rotor vibrations, two actuators with radial working directions can be positioned perpendicular to each other if necessary [**7**].

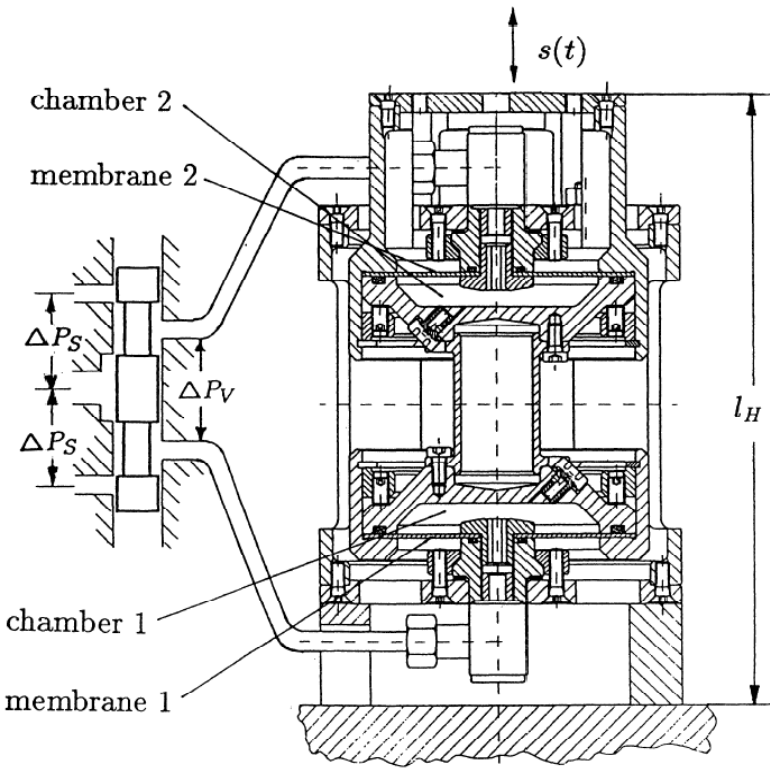

Figure 15 Cross-section of a hydraulic actuator [7].

An *active magnetic bearing* can be applied as a non-intrusive actuator in addition to its traditional function as a bearing that supports load through the use of magnetic forces. This type of actuator is utilized in this thesis to apply harmonic force to the shaft. An AMB utilizes electromagnets to apply only pulling forces to maintain the position of a rotor through the use of position sensors to monitor shaft position and a controller to direct proper current magnitudes to the electromagnet in real time. This is a non-intrusive means of applying force to a rotating body that can be controlled to provide stable rotor levitation. In an AMB, the distinguishing feature is that there is no physical contact between the rotor and the bearing stator which allows for relative motion of the shaft without any friction or wear.

In order for an AMB to operate, it requires an electromagnet assembly, a power amplifier, a controller, and a gap sensor as illustrated in Figure 16. During operation, a sensor continuously monitors the position of the rotor to provide feedback to the controller. With the updated gap information, the controller can supply the appropriate amount of current to the electromagnet, via the power amplifier, to control the magnetic force required to maintain the rotor in the desired position.

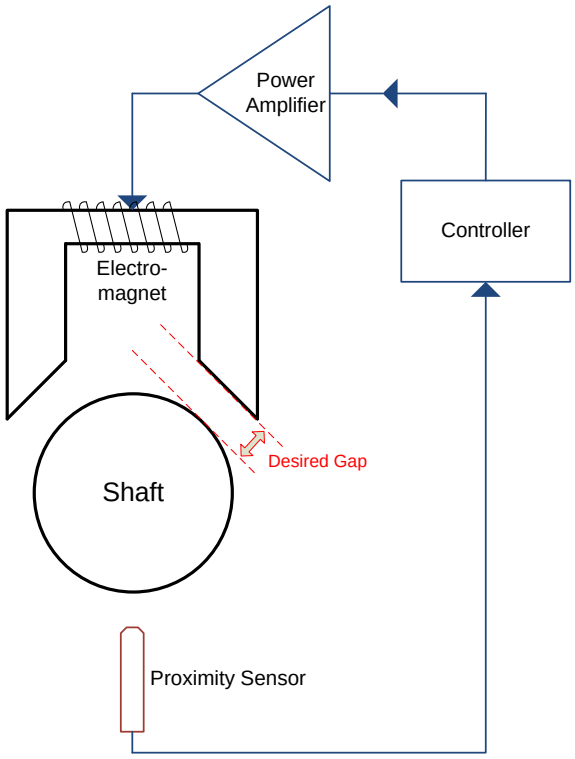

Figure 16 Conceptual diagram of an active magnetic bearing (AMB).

AMBs have been implemented to work in compressors, turbines, pumps, motors, and power generators which can apply to a variety of application such as petroleum refining, machine tool operation, electric power generation, natural gas pipelines,

precision instruments, and even maglev trains. Magnetic bearings have many advantages such as operating lubrication free, contamination free, friction free, and many more not listed for brevity. These features allow an AMB to run virtually wear free, clean, and with reduced vibrations when special control techniques are enabled. Rotating machines equipped with AMBs are capable of system/parameter identification, diagnosis and adaptive control action which lead to not only the higher performance of machines, but increase the reliability and thus increased service life [**9**]. Many magnetic bearing systems have Active Vibration Control (AVC) capabilities which notably reduce vibration amplitudes in real time. Rotor systems that may not be able to tolerate larger vibration amplitudes would greatly benefit from AVC to decrease vibration magnitudes. The main disadvantages include relatively high initial costs and larger size and weight compared with some other traditional bearings. However, for the application of a non-intrusive, contact free actuator as needed for this research, the AMB is the ideal candidate.

2.5 Literature Review

Research on the topic of transverse shaft crack has been underway for decades and has been presented in a number of published works, such as [**26-30**]. These works have been focused on the study of dynamic behavior of rotors with the so-called breathing type crack for either a predetermined speed or during the passage through a critical speed at constant angular acceleration or deceleration. These methods are all based on vibration monitoring because many machine faults are diagnosed with vibration

pattern changes. Continuation of this research has been motivated by the large financial incentive to keep machinery operating properly for longer periods of time with great reduction in unexpected failures. Much of this research has been successful in determining vibration pattern changes in common faults such as the ones described in Section 2.3 and are universally accepted in the rotating machinery community. A few examples relevant to this topic are presented in coming paragraphs.

Gasch [**14**] provided a comprehensive investigation of the stability behavior of a cracked Jeffcott rotor. The cracked shaft analysis of Gasch assumed a constant rotational speed and a forced vibration resulting from the system's residual unbalance. Furthering the investigation of cracked rotors, Iwatsubo *et al.* [**12**] used an external excitation technique to analyze the response of the cracked shaft. He showed the presence of combination harmonics due to interaction between impact force and rotation of shaft as the crack indicators. The concept of combination harmonic frequencies will be further presented in this thesis.

Sawicki *et al.* [**15**] [**16**] studied the dynamics of accelerating cracked rotors, and the application of nonlinear dynamics tools for crack diagnosis. The dynamic response of a cracked Jeffcott rotor passing through the critical speed with constant acceleration is investigated analytically and numerically. The nonlinear equations of motion that are derived include a simple hinge model for small cracks and Mayes' modified function for deep cracks. The effects of different factors such as various crack depths, acceleration, damping, torque, unbalance eccentricity, and rotor weight on the rotor vibrational response are studied. Vibration phase response is used as one of possible tools for detecting the existence of cracks. The results of parametric studies of the effect of crack

depth, unbalance eccentricity orientation with respect to crack, and the rotor acceleration on the rotor's response are presented.

Sinou and Lees [**17**] present works that investigate the influence of transverse cracks in rotating shafts. In particular, the paper addresses issues of the changes in modal properties and the influence of crack breathing on dynamic response during operation. Further investigations present modeling of the evolution of the orbit of a cracked rotor near half of the first resonant frequency. Expanding upon this work, Sinou and Lees [**18**] further investigate the rotor's response due the crack's opening and closing nature and examine the evolution of the orbit at half and one-third of first resonant frequency. The dynamic response of the cracked rotor is evaluated by expanding the changing stiffness of the crack as a truncated Fourier series and then using the Harmonic Balance Method. This allows for the examination of distinguishing features of a cracked rotor.

Ishida and Inoue [**19**] present an investigation on detection of a rotor crack based on the nonlinear vibration diagnosis using a harmonic excitation force. The open-close mechanism of crack is firstly modeled by a piecewise linear function. In addition, another approximation crack model using a power series function that is convenient for the theoretical analysis is used. In this research, a swept harmonic excitation force is applied to the cracked rotor and the nonlinear resonances due to crack are investigated. The occurrence of various types of nonlinear resonances due to crack are clarified and many of their characteristics are shown both numerically and experimentally.

Work done by Quinn et al. [**20**] models and experimentally verifies the presence of combinational resonances with the application of an AMB to apply excitation forces. The experiment is performed with the shaft supported on conventional ball bearings, and

the active magnetic bearing (AMB) is used in a mid-shaft or outboard location as an actuator to apply specified, time-dependent forcing on the system. In this work, it is shown that if these forces are properly chosen, they will induce a combination resonance that can be used to identify the magnitude of the time-dependent stiffness arising from the breathing mode of the shaft crack. The technique is verified experimentally on a high speed test rotor with a healthy and a cracked shaft and demonstrates that the response amplitude at the first natural frequency due to an applied excitation force at the identified combination resonance increases as the crack depth increases.

Bash [**21**] presented research utilizing an AMB to excite a rotating shaft, where the objective was to incorporate an AMB into an existing, conventionally supported (ball) bearing rotor system to diagnose faults in a shaft. This technique would not be limited to magnetically levitated systems which are not as common as conventionally supported systems. An AMB placed in a near mid-shaft location is used only as a non-load bearing magnetic actuator to aid in detection of a shaft crack. Similar to modal analysis and other nondestructive evaluation (NDE) techniques, this work follows the approach which allows for the measurement of both input and output response in a rotating system for evaluation. However, unlike these techniques, a new procedure presented in this research allows for multiple forms of force input signals to be applied to a rotating structure. In an effort to help justify the presence of AMBs, Bash mentions other possible functions of such hardware. For example, AMBs can operate as magnetic dampers for the reduction of up to three modes of rotor synchronous vibration [**21**]. This paper presents the results from this project which includes both shaft rub and notch. An EDM notch was also tested to attempt a breathing scenario similar to breathing cracks.

CHAPTER III

MODELING OF CRACKED ROTOR SYSTEMS

3.1 Introduction to the Breathing Crack

The breathing transverse shaft crack is tied to the key concept of weight dominance. This means that the shaft sags below the bearing centerline due to its own weight. Further, the entire shaft orbit remains below the bearing centerline during rotation to fulfill this criterion. Figure 17 illustrates an exaggerated image of shaft sag. When this is the case, the transverse shaft crack is forced to open and close with every shaft revolution due to the shaft's bending. However, in the case where rotor vibration amplitudes exceed the magnitude of shaft sag due to gravity, the crack may not open and close predictably which may not produce parametric excitation.

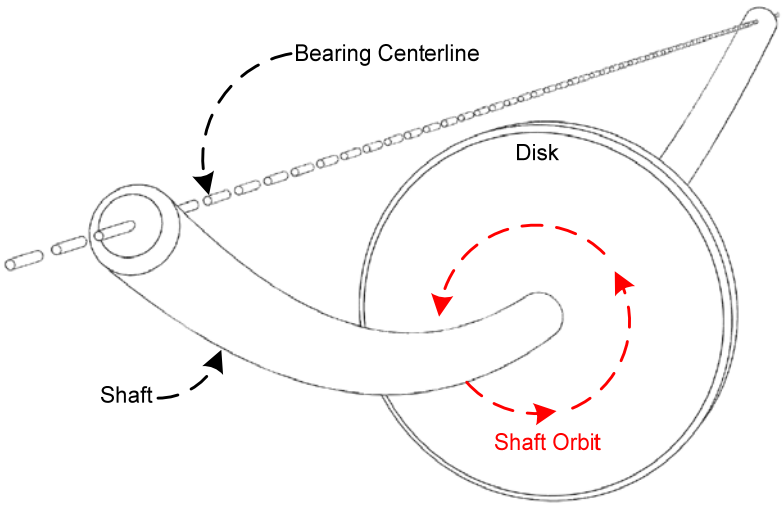

Figure 17 Illustration of the weight dominance concept.

For reference, the vertical direction opposite of gravity will be referred to as 0°. Figure 18 shows the progression of the crack opening and closing due to weight dominance as the shaft rotates. The crack's fully closed position is shown as the starting point at 0°. In this orientation, the crack is in a compressive state and does not reduce the shaft's stiffness. As the shaft rotates 180°, the crack moves to the fully open state where the shaft achieves its maximum stiffness reduction. Any crack orientation between the fully closed and fully open positions provides some intermediate shaft stiffness reduction. When completing the shaft rotation to 360°, the crack will be in the fully closed orientation and the cycle repeats.

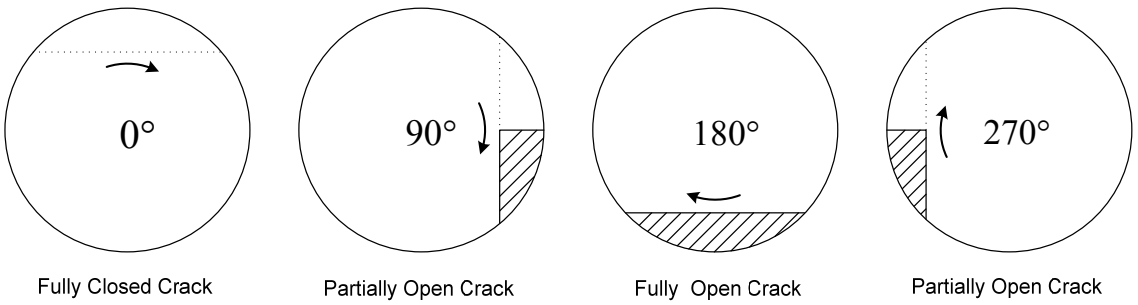

Figure 18 Cycle of crack opening and closing due to weight dominance.

In the development of the equations of motion for rotor-bearing systems, one needs to define coordinate systems to quantify the position of the crack on the shaft. In order to do this, a coordinate system that is either inertial (fixed in space) or rotating (fixed to the spinning rotor) must be chosen. Generally, if the bearings and supports are isotropic, the analysis of the system with cracked (asymmetric) rotor is best performed in rotating coordinates. In this case, the resulting second order differential equations of motion have constant coefficients and produce a standard eigenvalue problem. When both the rotor and the bearings and support structure contain asymmetries, then the resulting equations of motion contain time dependent parameters. The parameters vary sinusoidally and produce an effect referred to as parametric excitation [**22**], occurring in both the inertial and rotating frames, independent of the coordinate system used. In this case, the problem cannot be solved using a standard eigenvalue problem and stability must be determined using Floquet theory [**23**]. Finally, it should be mentioned that if the rotor is symmetric then the analysis is best performed in coordinates that are inertial, regardless if the bearings and supports are isotropic or not.

3.2 Equations of Motion of Cracked Rotor

Usually, the supports of rotors exhibit higher stiffness vertically than horizontally, especially in the case of large machines. Thus there is no compelling reason to use fixed or rotating coordinates for the analysis. To determine the stiffness of the rotor as the crack opens and closes, it is easier to work in coordinates that are fixed to the rotor which rotate with it. The reduction in stiffness due to a crack is then calculated in directions perpendicular to and parallel to the crack face, and these directions will rotate with the rotor. Having determined the rotor stiffness in rotating coordinates, the stiffness matrix is transformed to fixed coordinates and joined to the system inertia to obtain the equation of motion in fixed coordinates.

Let the stiffness matrix for the un-cracked rotor in rotating coordinates be $\tilde{\mathbf{K}}_0$ and the reduction in stiffness due to a crack be $\tilde{\mathbf{K}}_c(\theta)$, where θ is the angle between the crack axis and the rotor response at the crack location and determines the extent to which the crack is open. Thus the stiffness of the cracked rotor in rotating coordinates is:

$$\tilde{\mathbf{K}}_{cr} = \tilde{\mathbf{K}}_0 - \tilde{\mathbf{K}}_c(\theta) \tag{1}$$

This stiffness matrix is transformed from rotating to fixed coordinates using the transformation matrix $\mathbf{T}(\Omega t)$, shown as:

$$\mathbf{T}(\Omega t) = \begin{bmatrix} \cos(\Omega t) & \sin(\Omega t) \\ -\sin(\Omega t) & \cos(\Omega t) \end{bmatrix} \tag{2}$$

When assuming the un-cracked rotor is axi-symmetric, and then transforming it to non-rotating coordinates, the equation results in:

$$\mathbf{K}_{cr} = \mathbf{T}^{\mathrm{T}}\tilde{\mathbf{K}}_0\mathbf{T} - \mathbf{T}^{\mathrm{T}}\tilde{\mathbf{K}}_c(\theta)\mathbf{T} = \mathbf{K}_0 - \mathbf{K}_c(\theta,t) \tag{3}$$

Let the deflection of the system be $\mathbf{q} = \mathbf{q}_{st} + \mathbf{q}_{dy}$ where $\mathbf{q}_{st}$ is the static deflection of the un-cracked rotor due to gravity, and $\mathbf{q}_{dy}$ is the dynamic deflection due to the rotating out of balance and the effects of the crack. Thus, the equation of motion for the rotor in fixed co-ordinates is:

$$\mathbf{M}\ddot{\mathbf{q}}_{dy} + (\mathbf{D}+\mathbf{G})\dot{\mathbf{q}}_{dy} + (\mathbf{K}_0 - \mathbf{K}_c(\theta,t))(\mathbf{q}_{st} + \mathbf{q}_{dy}) = \mathbf{Q}_u + \mathbf{W} \tag{4}$$

where $\mathbf{Q}_u$ and $\mathbf{W}$ are the out of balance force and the gravitational force, respectively. Damping and gyroscopic effects have been included as a symmetric positive semi-definite matrix $\mathbf{D}$ and a skew-symmetric matrix $\mathbf{G}$, even though they have little direct bearing on the analysis. If there is axi-symmetric damping in the rotor then there will also be a skew-symmetric contribution to the undamaged stiffness matrix, $\mathbf{K}_0$. Equation (4) is the nonlinear equation of motion and it will be referred to as the "full equation".

The steady state deflection of the rotor varies over each revolution of the rotor since $\mathbf{K}_c$ varies. However, the stiffness reduction due to the crack is usually small, and we may make the reasonable assumption that $\|\mathbf{K}_0\| \gg \|\mathbf{K}_c(\theta,t)\|$. With this assumption, the steady state deflection is effectively constant and equal to the static deflection, $\mathbf{q}_{st}$, given by:

$$\mathbf{K}_0\mathbf{q}_{st} = \mathbf{W} \tag{5}$$

Equation (4) then becomes:

$$\mathbf{M}\ddot{\mathbf{q}}_{dy} + (\mathbf{D}+\mathbf{G})\dot{\mathbf{q}}_{dy} + (\mathbf{K}_0 - \mathbf{K}_c(\theta,t))\mathbf{q}_{dy} = \mathbf{Q}_u \tag{6}$$

The second approximation commonly used in the analysis of cracked rotors is weight dominance. Most rotating machines can be considered weight dominated which means that the static deflection of the rotor is much greater than the dynamic response due to the unbalance or rotating asymmetry, that is $|\mathbf{q}_{st}| \gg |\mathbf{q}_{dy}|$. In this situation, the crack opening and closing is dependent only on the static deflection and thus $\theta = \Omega t + \theta_0$, where Ω is the rotor speed and θ_0 is the initial angle. Thus Equation (6) becomes:

$$\mathbf{M}\ddot{\mathbf{q}}_{dy} + (\mathbf{D}+\mathbf{G})\dot{\mathbf{q}}_{dy} + (\mathbf{K}_0 - \mathbf{K}_c(t))\mathbf{q}_{dy} = \mathbf{Q}_u \tag{7}$$

where $\mathbf{K}_c$ is now independent of θ. Since the stiffness matrix in stationary coordinates $\mathbf{K}_c(t)$ is a periodic function of time only, the full nonlinear Equation (4) becomes the linear parametrically excited Equation (7).

3.3 The Model for Breathing Crack

The opening and closing or "breathing" of the crack as the rotor rotates results in a periodic change in rotor stiffness. The kinematics of the cracked shaft is shown in the Figure 19.

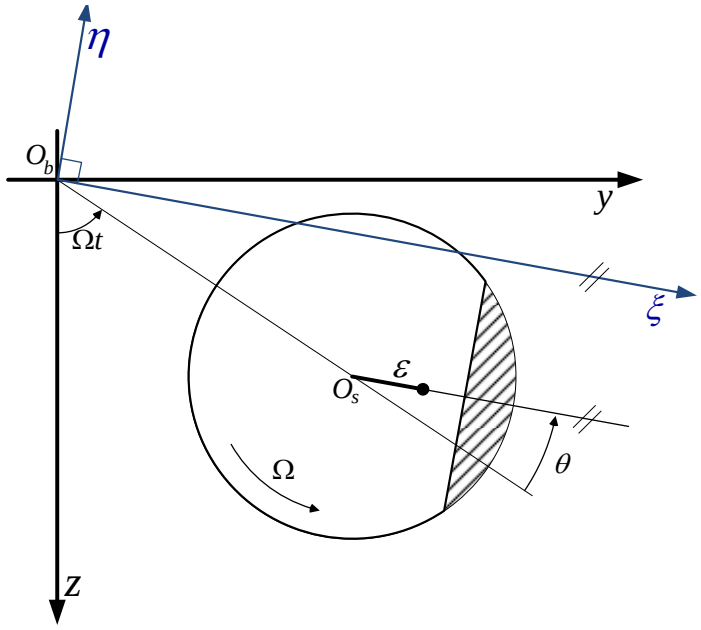

Figure 19 Shaft and crack position described in inertial and rotating coordinate systems [24].

For small cracks, the rectangular function from the hinge model is used which describes the crack's sudden opening and closing, by switching from 1 (open) to 0 (closed). This function can be approximated by the Fourier expansion as follows:

$$f(\theta) = \frac{1}{2} + \frac{2}{\pi}\cos\theta - \frac{2}{3\pi}\cos 3\theta + \frac{2}{5\pi}\cos 5\theta - \ldots \tag{8}$$

In the case of deep cracks, there is a smooth transition between the opening and closing of the crack and this is reflected by the Mayes' modified function, i.e.,

$$f(\theta) = \frac{1+\cos\theta}{2} \tag{9}$$

In this thesis the fully open crack is modeled by reducing the element stiffness in orthogonal directions (parallel and perpendicular to the crack face). The stiffness matrix

of the rotor when the crack is open, in rotating co-ordinates, is then $\tilde{\mathbf{K}}_1$. If weight dominance is assumed, then the opening and closing of the crack is periodic at the rotor spin speed. In the Mayes model the time dependent stiffness matrix in rotating coordinates is:

$$\tilde{\mathbf{K}}_c(t) = 0.5 \times \left(1 - \cos\left(\Omega t + \theta_1\right)\right)\left[\tilde{\mathbf{K}}_0 - \tilde{\mathbf{K}}_1\right] \tag{10}$$

where θ_1 depends on the crack orientation and the initial angle of the rotor. When $\cos\left(\Omega t + \theta_1\right) = 1$, the crack is fully closed and $\tilde{\mathbf{K}}_{cr}(t) = \tilde{\mathbf{K}}_0$, the un-cracked rotor stiffness, where $\tilde{\mathbf{K}}_{cr}$ is defined in Equation (1). Thus the rotor is axi-symmetric when the crack is closed. When $\cos\left(\Omega t + \theta_1\right) = -1$ the crack is fully open so that $\tilde{\mathbf{K}}_{cr}(t) = \tilde{\mathbf{K}}_1$. Note that when the crack is open the rotor is asymmetric.

Converting from rotating to fixed co-ordinates is performed using the transformation given in Equation (3). The stiffness matrix in stationary co-ordinates, $\mathbf{K}_c(t)$, is a periodic function of time only and the full non-linear Equation (4) becomes a linear parametrically excited equation. Penny and Friswell [**25**] showed that the model generates a constant term plus 1X, 2X, and 3X rotor angular velocity components in the stiffness matrix.

3.4 Health Monitoring Using External AMB Force Excitation

Recently a number of authors have considered the use of AMBs as a force actuator that is able to apply force to the shaft of a machine [**13**][**20**][**21**][**26**][**27**]. If the applied force is periodic, then the presence of the crack generates responses containing

frequencies at combinations of the rotor spin speed and applied forcing frequency. The excitation by unbalance and AMB forces produces *combinational frequencies* between critical speeds of the shaft, the rotor spin speed, and the frequency of the AMB excitation. The key is to determine the correct excitation frequency to induce a *combinational frequency* that can be used to identify the magnitude of the time-dependent stiffness arising from the breathing mode of the rotor crack.

The force applied on the rotor by the AMBs must be included in the equations of motion. Thus Equation (7) becomes:

$$\mathbf{M}\ddot{\mathbf{q}}_{dy} + \left(\mathbf{D}+\mathbf{G}\right)\dot{\mathbf{q}}_{dy} + \left(\mathbf{K}_0 - \mathbf{K}_c\left(t\right)\right)\mathbf{q}_{dy} = \mathbf{Q}_u + \mathbf{Q}_{\text{AMB}} \tag{11}$$

where $\mathbf{Q}_{\text{AMB}}$ is the external forces applied to the rotor by the active magnetic bearing. This force will be chosen to be harmonic, either in one or two directions, although other waveforms would be possible.

The key aspect of the analysis is that the system has three different classes of frequencies, namely the natural frequencies (or critical speeds), rotor spin speeds, and the forcing frequencies from the AMB. The parametric terms in the equations of motion (or non-linear terms in the full equations) cause *combinational frequencies* in the response of the machine. Mani et al. [**27**] and Quinn et al. [**20**] used a multiple scales analysis to determine the conditions required for a combinational resonance, which occurs when:

$$\Omega_{AMB} = \left|n\Omega - \omega_n\right|, \qquad \text{for} \quad n = \pm 1, \pm 2, \pm 3 \tag{12}$$

where Ω is the rotor spin speed, Ω_{AMB} is the frequency of the AMB force, and ω_n is the natural frequency of the system.

3.5 Brief Simulation Case Study

A case study of a simple rotor is performed to demonstrate the application of the finite element method using the modeling concepts described in previous sections. The following example illustrates the effect of the transverse crack as well as the effect of an AMB actuator applying a harmonic excitation force with a particular frequency. The FFT spectrum results show that the crack induces an array of combination frequencies in addition to the AMB injection frequency.

The finite element model used in this case study is shown in Figure 20. It is composed of 6 elements, 7 nodes, and two disks as well as bearings located at nodes 1 and 7, a 40% cracked element, and AMB excitation at node 3. The shaft is 5/8" in diameter and 17.25" in length, divided equally into 6 elements. The 5" disk is 1" thick and is located at node 4 and the 3" disk is ½" thick and is located at node 5. Ball bearing stiffness is roughly calculated to be 30 MN⁄m in all radial directions derived from Equation (14) with damping values assumed to be 10 N·s⁄m. The AMB force is estimated to be 10 N which is derived from Equation (13). The rotor has a modeled unbalance of 0.001 kg·m located at node 4 and is composed of material properties for average stainless steel which are as follows; E = 206.8 GPa, ν = 0.3, G = 82.7 GPa, and ρ = 7888 kg⁄m^3 .

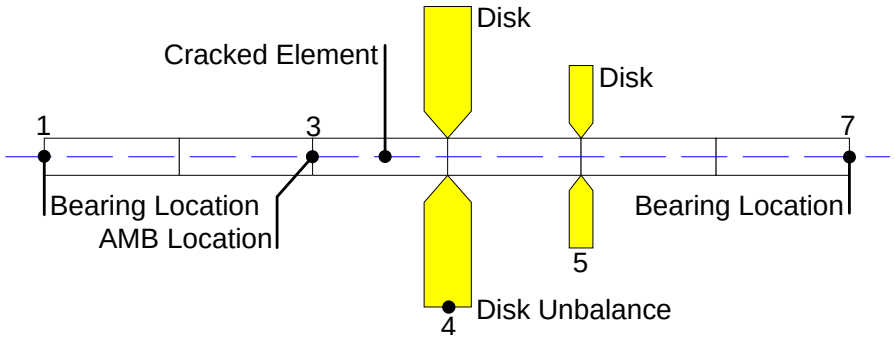

Figure 20 Simple finite element model with two disks for case study only.

The rotor characteristics of this system are shown in Figure 21. The left side of the figure shows the unbalance response up to 40,000 rpm which includes the first two critical speeds. The right side of the figure illustrates the corresponding Campbell diagram which also shows the first two critical speeds at the intersection of the dotted line. From this figure, it is clear that the first critical speed is located at 54 Hz which is necessary information for the combination frequency equation. Although any critical speed can be used in that equation, this thesis only investigates the use of the first due to the speed limitations of Cleveland State's rotor crack detection test rig.

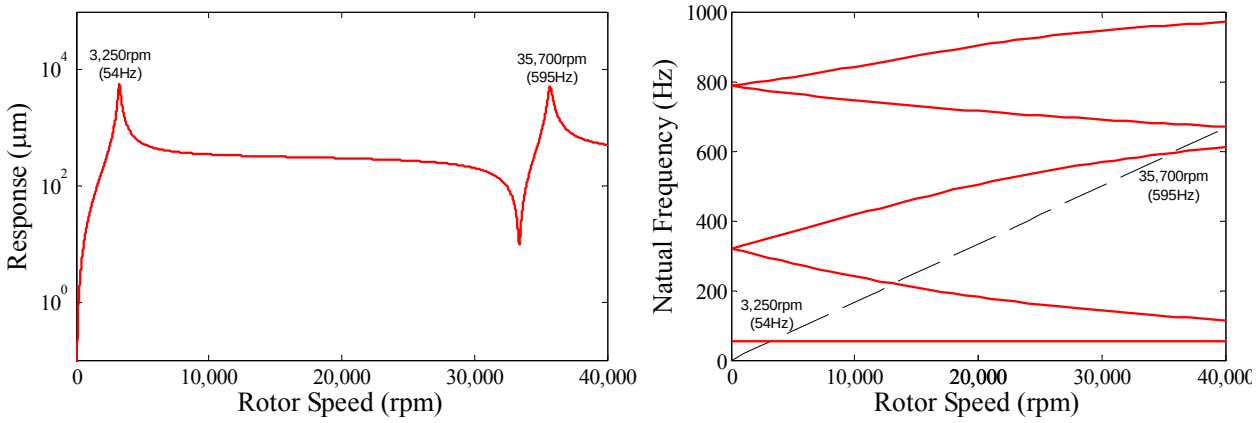

Figure 21 *Left:* Unbalance response simulation. *Right:* Campbell diagram.

When using the combination frequency Equation (12), it is necessary to provide a critical speed, an n value, and the running speed. For this case, the first critical speed is 54 Hz, an arbitrarily chosen n value is 2, and the running speed is 0.75×54 Hz = 40.5 Hz. It was found through experimenting with various running speeds that it is most effective when it is 75% of the first critical speed. However, it should be noted that other possibilities exist. At this speed, all combination frequencies are evenly spread throughout the frequency spectrum. This is not only visually appealing, but also provides a smaller chance of combination frequency peaks overlapping and/or contaminating each other. Refer to Figure 24 for further description. Table 1 provides a listing of all combination frequencies when applied to this system. The shaded row shows the *n* value of 2 and the corresponding 27 Hz AMB injection frequency. All other combination frequencies appear as peaks in the FFT plots when AMB excitation is applied and are shown in *italics*.

***n* value**	**Ω (Hz)**	**ω_n (Hz)**	**Ω_{AMB} / Combination Frequency (Hz)**
-3	40.5	54	175.5
-2	40.5	54	135
-1	40.5	54	94.5
0	40.5	54	54
1	40.5	54	13.5
2	**40.5**	**54**	**27**
3	40.5	54	67.5
4	40.5	54	108
5	40.5	54	148.5
6	40.5	54	189

Table 1 Combination frequencies for corresponding *n* values.

The simulation in Figure 22 shows the FFT spectrum of a healthy shaft. The top FFT plot shows the case where there is no injection which results in only the running speed or a 1X component. The lower FFT plot in this figure shows the case there is an injection of 27 Hz which results in a spectrum containing the 1X component as well as the injection frequency.

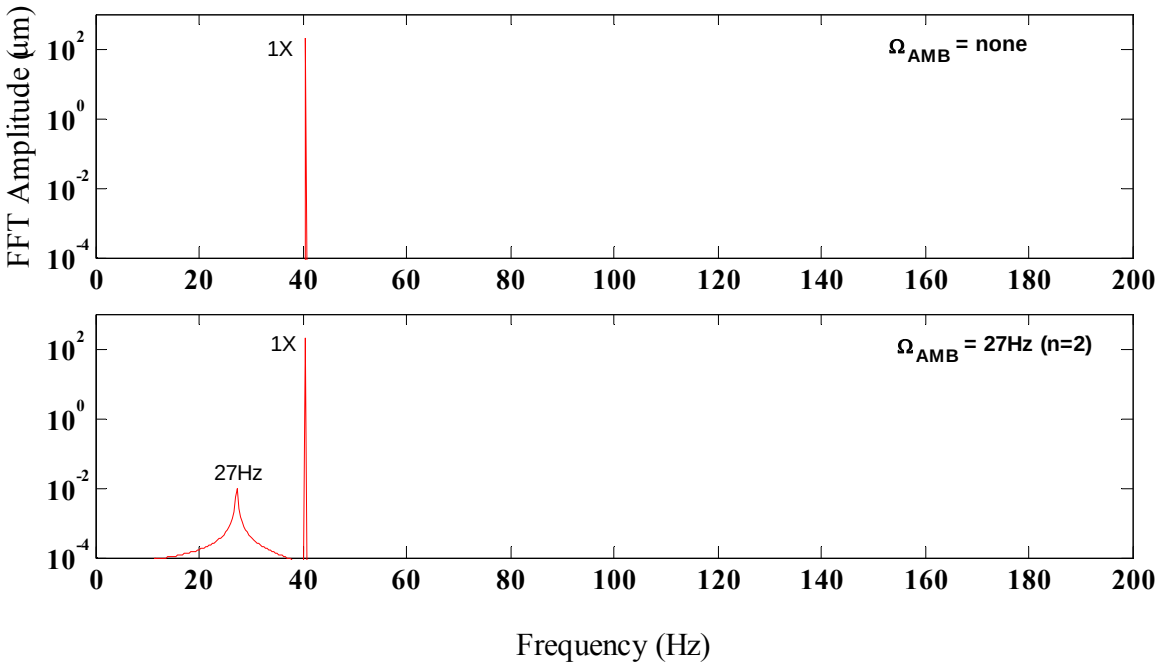

Figure 22 Simulated responses for the healthy rotor. Ω=40.5 Hz, external force of 10 N with and without injection.

The simulation in Figure 23 shows the FFT spectrum of the 40% cracked shaft. The top FFT plot shows the case where there is no injection which results in the running speed or a 1X component and its multiples, 2X, 3X, and 4X due to the presence of the crack.

The lower FFT plot in this figure shows the case there is an AMB injection of 27 Hz which results in a spectrum containing the 1X component, its multiples, 2X, 3X, and 4X, and the injection frequency. In addition, this case shows the presence of all the combination frequencies listed in Table 1 which are labeled in *italic* on the plot. This is due to the existence of the crack in combination with the AMB force injection of 27 Hz. This force injection excites all the combination frequencies when a crack is present. In theory, the rotor response should only be non-zero at only these frequencies; however, leakage has caused some energy to spread into neighboring frequencies.

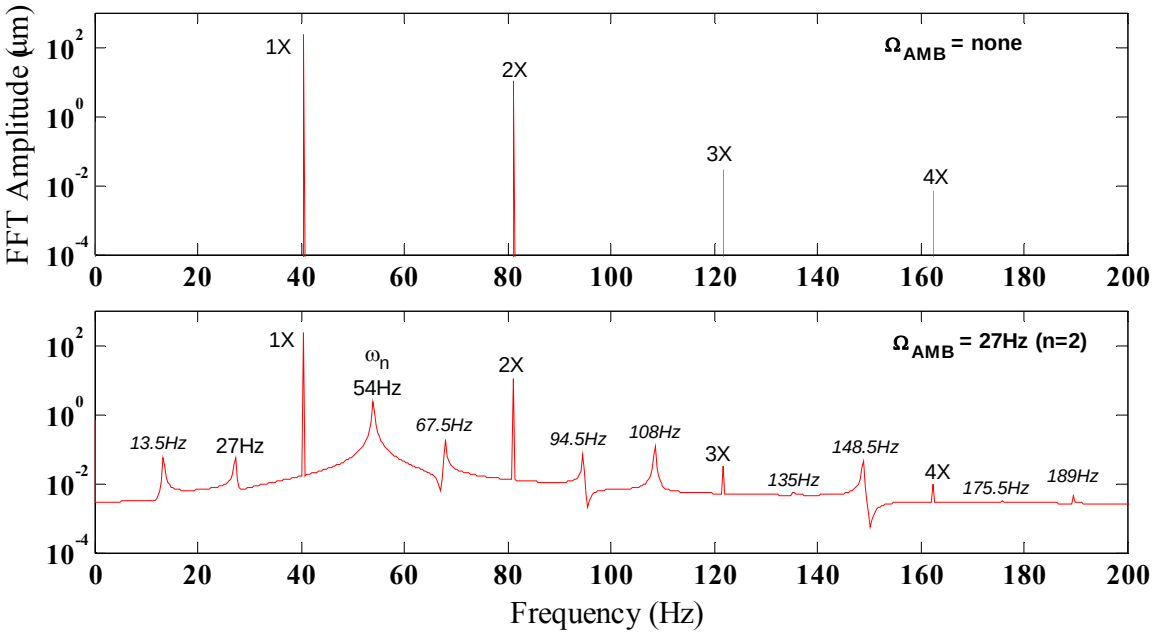

Figure 23 Simulated responses for the rotor with a 40% crack. Ω=40.5 Hz, external force of 10 N with and without injection.

To aid explanation for using a running speed 75% of the critical speed, Figure 24 illustrates the simulated FFT plot of the same finite element model but with a running speed 95% of the critical speed. This FFT plot is calculated using the 40% cracked shaft

and AMB injection of 48.6 Hz. Note that by changing the running speed, the AMB injection frequency changes while still using an *n* value of 2. It is obvious that the combination frequencies are excited due to the AMB injection, however, they are merging into each other producing unclear results. This merging of combination frequency peaks may not be easily seen in experimental data and is why the selection of the running speed is 75% of critical speed.

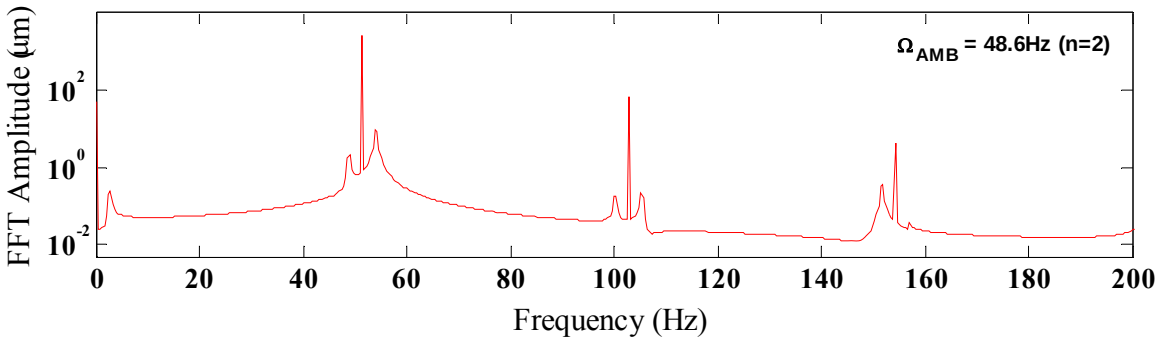

Figure 24 Simulated responses for the rotor with a 40% crack. Running speed 95% (Ω=51.3 Hz) of first critical speed.

CHAPTER IV

EXPERIMENTAL SETUP AND PROCEDURE

4.1 Crack Detection Test Rig

The experimental crack detection test rig used in this work was built by Revolve Magnetic Bearing Inc™ and consists of a base plate, three AMBs with rotors, a motor, a shaft, and a balance disk. Additionally, a SKF™ PID controller, necessary for levitated AMB operation, is coupled to MBScope 2000™ software installed on a PC which is required for parameter control. This is a complete system that can magnetically levitate the rotor and, consequently, monitors rotor performance with the built in proximity probes housed in the each of the three AMBs.

A dSPACE™ data acquisition system is connected to the AMB proximity probes which provides more flexibility in data collection but is strictly used as a means of control over signal injection to the actuator AMB. See Section 4.3 for further review.

For data collection and processing, an ADRE® Sxp/408 DSPI Asset Condition Monitoring System described in Section 4.2 is used to monitor rotor performance instead of Revolve's™ MBScope 2000™ software or dSPACE™. This requires the use of additional Bently-Nevada® proximity probes that are mounted independently of the existing AMB proximity probes. In summary, Revolve's™ MBScope 2000™ software is used only for control of the motor speed, the dSPACE system controls signal injection in the actuator AMB, and the ADRE® Sxp/408 DSPI is used for data collection and processing. This is illustrated in a flow chart pictured in Figure 25.

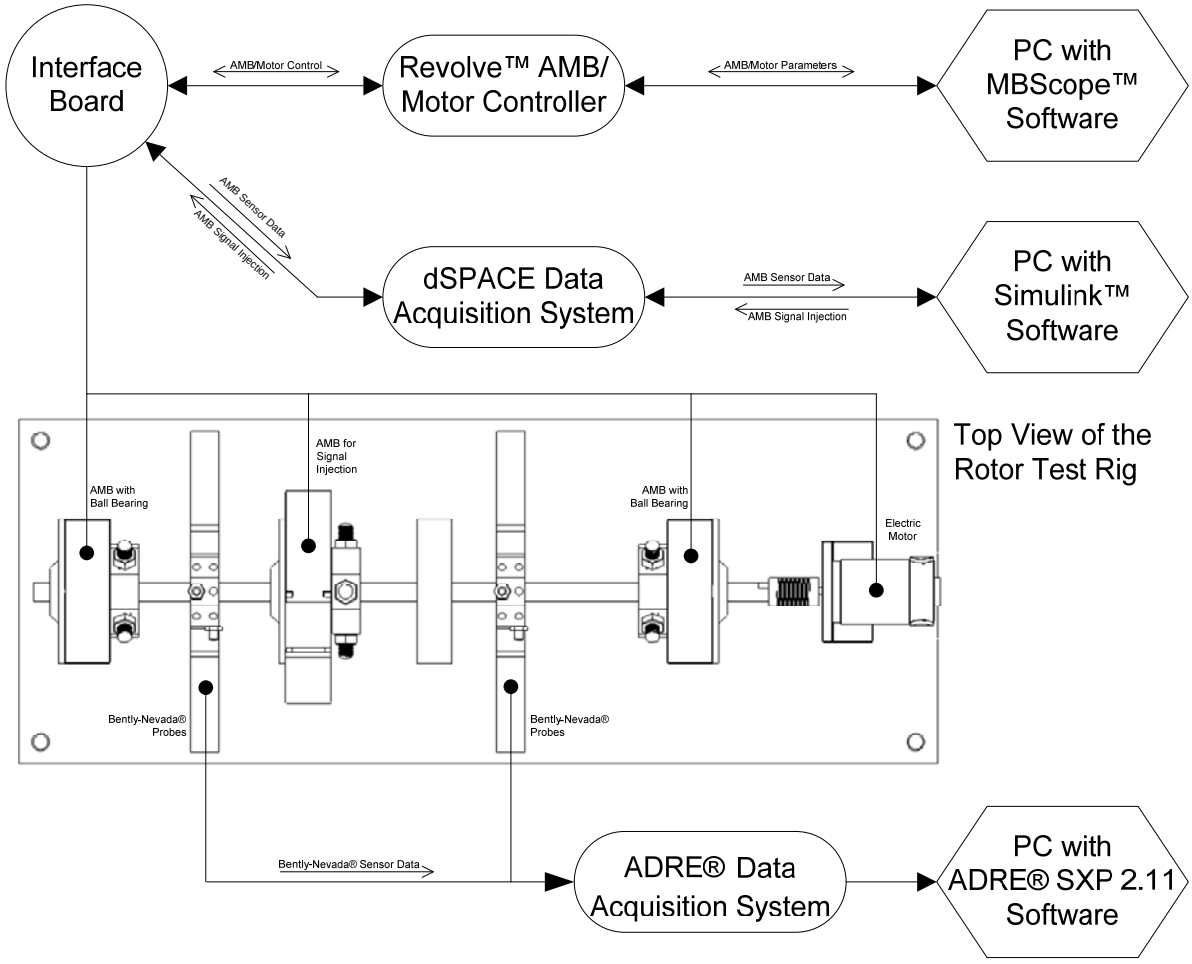

Figure 25 Top view of rotor test rig with system flow chart.

In the configuration shown in Figure 27, the shaft is supported by two ball bearings spanned 23" apart which are mounted to the AMBs via plates, located at both ends of the shaft. These two load supporting AMBs *do not* perform magnetic levitation. Two pairs of Bently-Nevada® proximity probes (connected to an ADRE® Sxp/408 DSPI) are positioned at horizontal and vertical positions where each pair is fixed to a mounting block for direct monitoring of the shaft which is shown in Appendix A. The AMB actuator is located in an approximate mid-span configuration in an effort to maximize its effectiveness.

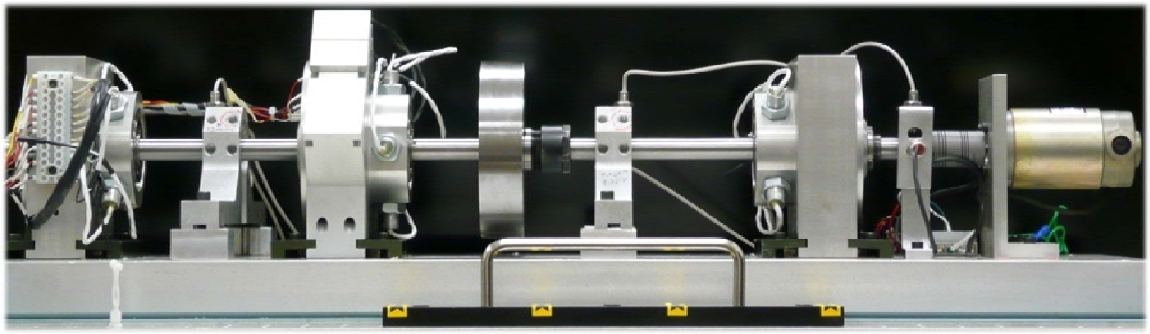

Figure 26 Photo of Cleveland State's rotor test rig.

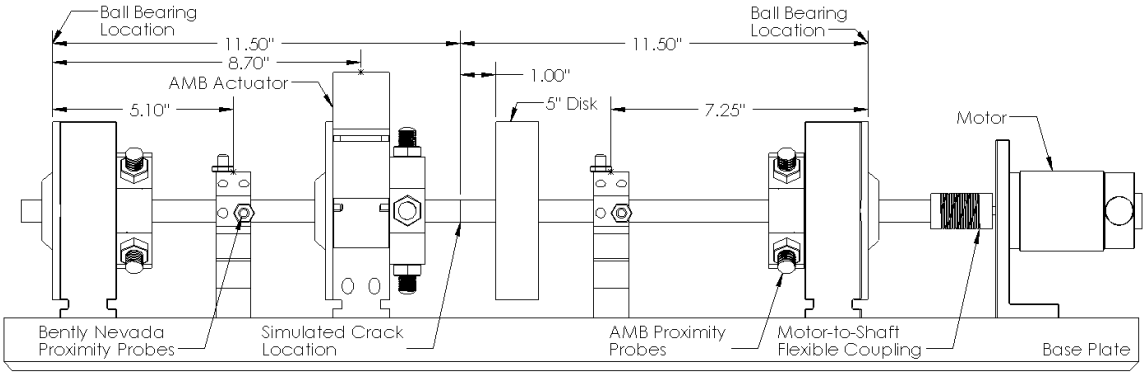

Figure 27 CAD drawing of Cleveland State's rotor test rig.

The rotor assembly itself consists of a shaft, disk, a cylindrical rotor, and two conical rotors as shown in Figure 28. A detailed drawing of the rotor is shown in Appendix A. The cylindrical and conical rotors are used by the AMBs in configurations where the shaft diameter is too small to provide adequate distance and surface area for the electromagnet to apply force to allow for levitation. In this case, the two conical rotors are not used for levitation; they are included for use with the AMBs' proximity probes to complete the system. The cylindrical rotor is necessary for use with the AMB force actuator to apply the specified excitation force to the rotor assembly.

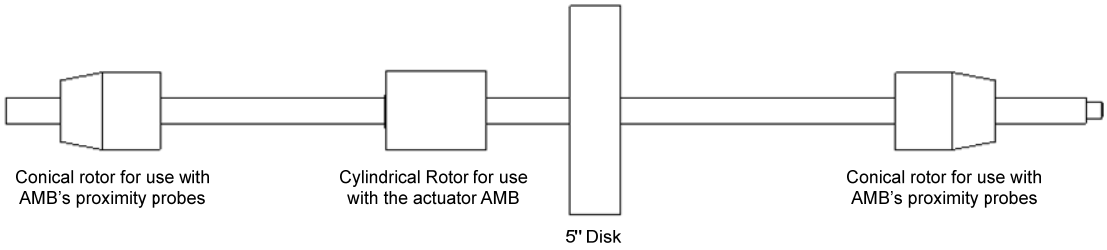

Figure 28 CAD drawing of the rotor only.

An experimental research is focused on simulation of the rotor with a breathing-type crack. However, it should be noted that a real crack has a virtually zero width and a reasonably unpredictable cross-section which was not possible to artificially recreate at our test facility. Further details on the shaft crack are provided in Section 4.1.2. The magnitude of "crack breathing" is dependent on the static deflection of the shaft which is essential to satisfy the weight dominance assumption. For this reason, the crack is located 11.5" from either bearing, where the most deflection occurs. Ideally, the disk would be placed in the same location, but due to an effort to isolate the crack and

minimize any unwanted interactions, the near face of the disk is located 1" from the crack. To confirm the magnitude and position of the point of maximum deflection of the shaft, the commercial finite element software, CosmosWorks™, was employed. Figure 29 shows that the maximum deflection due to gravity lands essentially in the center of the shaft where the crack is located having a resultant displacement of about 1.92×10^{-4} m or 0.00756". Note that deflection shape is not to scale for illustration purposes. The vertical dotted line in the figure is the location of the actuator AMB backup bearing. At this location, the shaft is statically deflected approximately 0.0063". The backup bearing has a clearance of ±0.0075" (explained in Section 4.1.1) which indicates that the weight dominance assumption is still valid. This means that the shaft orbit essentially remains below the bearing centerline to force breathing in the crack.

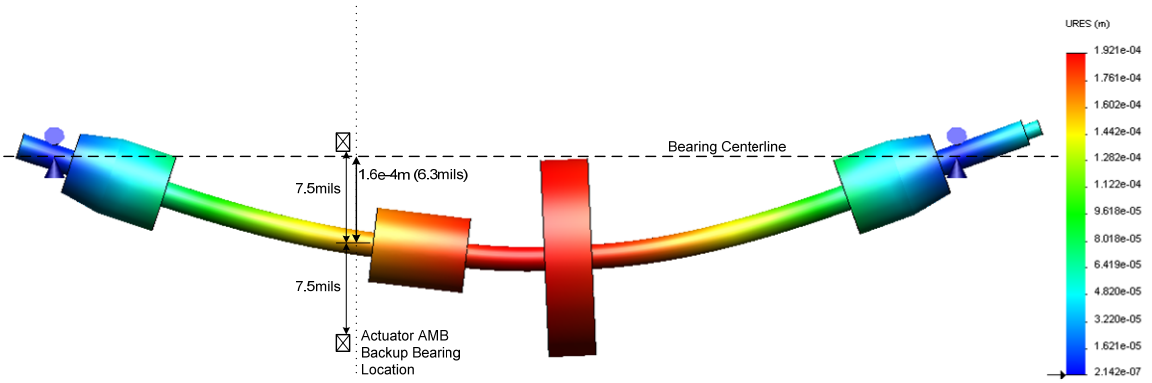

Figure 29 CosmosWorks™ FE model for static deflection due to gravity.

4.1.1 Revolve™ Active Magnetic Bearing Force Actuator

Unlike the two AMBs with ball bearings to support the shaft, the mid-span actuator AMB does not have a ball bearing for shaft support, which allows it to

magnetically apply a harmonic force to the shaft without any physical contact. This makes certain that any dynamic effects due to the direct contact from an actuator to the shaft are eliminated.

The Revolve™ AMB features an 8-pole heteropolar electromagnet with two axes of control, arranged to utilize four poles per axis. The axes are directed at 45˚ and 135˚ relative to horizontal and are designated by the letters V and W as shown in Figure 30. The clearance gap between the rotor and the stator is 0.015", while the gap between the backup bearing and the shaft is ±0.0075". In other words, when the shaft is in the concentric position in the actuator AMB, it has 0.0075" of travel in any direction before making contact with the backup bearing. The presence of the backup bearing, commonly a rolling element bearing, is essential for times when the rotor is not being levitated or in the event the rotor exceeds its operating limits. This prevents the rotor coming into contact with the stator which would potentially cause serious damage.

In this work, it is assumed desirable to inject the excitation force in a direction which will coincide to the shaft crack's breathing direction. Since the crack breathing is dictated by the shaft sag due to gravity, the direction of injection should follow. Because Revolve's™ AMBs are oriented with their axes tilted at 45˚ and 135˚, the actuator AMB was modified so that the axis are arranged at 0˚ and 90˚. Shown in Figure 30 on the right is a conceptual diagram of how the W axis on the actuator AMB is rotated 45˚ to provide vertical actuation corresponding to the direction of gravitational force. The actual AMB modification is shown in the schematic in Figure 31 which was machined and assembled at Cleveland State University.

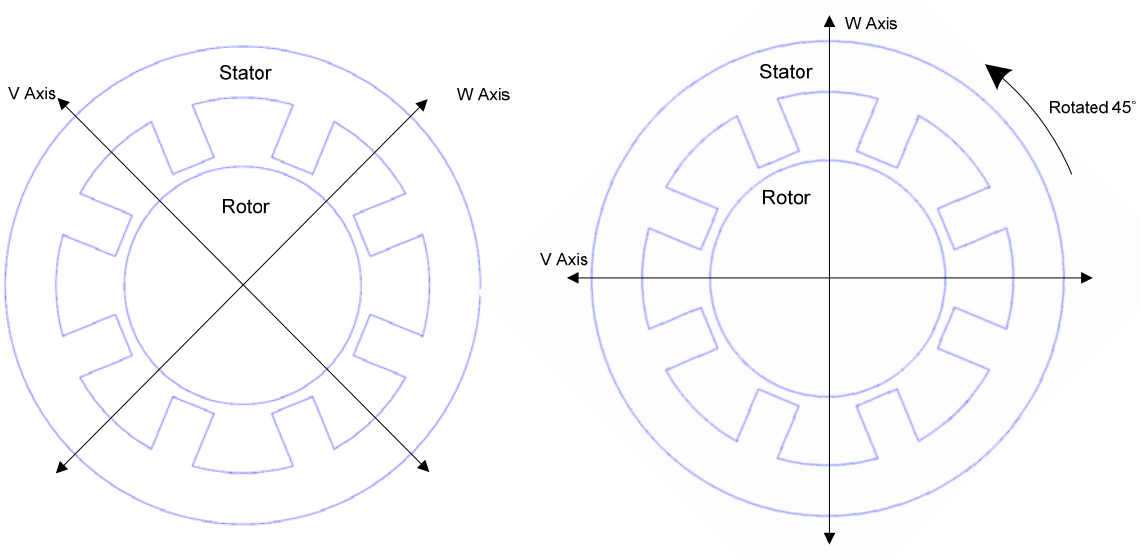

Figure 30 ***Left:*** **Original AMB configuration.** ***Right:*** **Modified AMB configuration.**

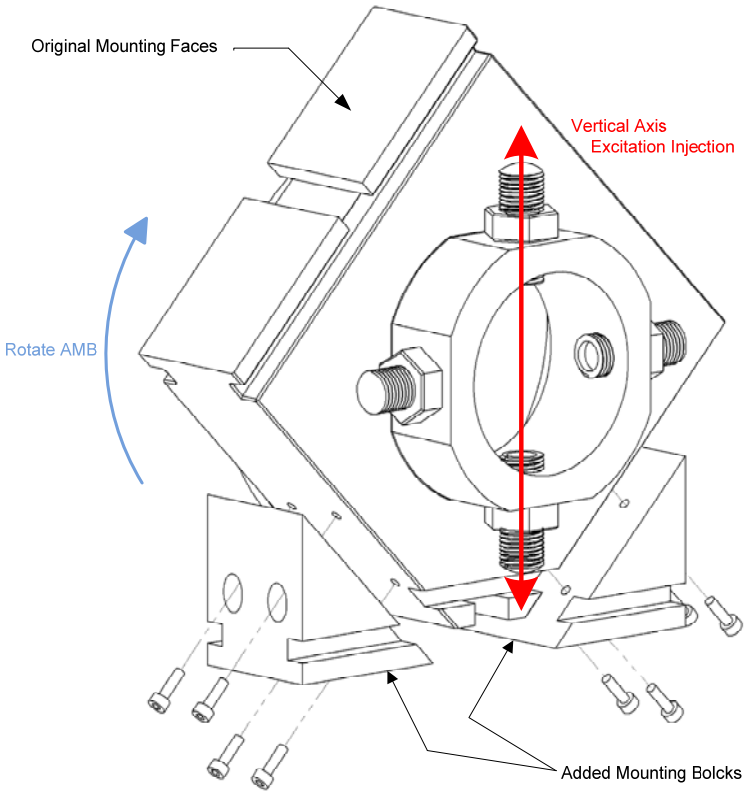

Figure 31 CAD drawing of the modified AMB.

An estimation of magnetic force is necessary for design of a magnetic bearing to assure that it will easily be able to levitate the rotor. The magnetic forces applied by an AMB are directly related to magnitude of the current in the stator coils, the air gap and inherent properties of the circuitry within the AMB. This means that the magnetic force from an AMB is dependent on several parameters. These parameters provide the necessary information to the control system for proper AMB operation. The force equation is shown below is used for calculation of an approximate force that the actuator AMB applies to the rotor.

$$F_{AMB} = C \times \left[\left(\frac{I_{top}}{2\left(g_{AMB} - x_{AMB}\right)} \right)^2 - \left(\frac{I_{bottom}}{2\left(g_{AMB} + x_{AMB}\right)} \right)^2 \right] \times 10^6 - F_{AMB_0} \qquad (13)$$

When applying this equation to the described system, AMB force values result in approximately 10 N. However, it should be noted that this values changes depending on the instantaneous position of the shaft which changes at a high rate. This value will only be used for modeling purposes Section 3.5.

4.1.2 Other Rig Components

The *5/8" diameter shafts* used in this rotor test rig are custom made from 416 hardened stainless steel and have been ground to an average straightness tolerance of ±0.0007" deflection per 26" length. One end of the shaft has a 0.375" long by 0.375" diameter section where the motor-to-shaft coupling is attached. On the same end, a keyway is machined which is used by the keyphasor connected to the SKF™ motor controller.

In this research, three shafts are used to obtain all necessary measurements and data. Illustrations of the cross-sections are shown below in Figure 32 and a listing of the three shafts used is as follows:

Shaft 1: Healthy, un-cracked shaft

Shaft 2: 25% deep EDM cut

Shaft 3: 40% deep EDM cut

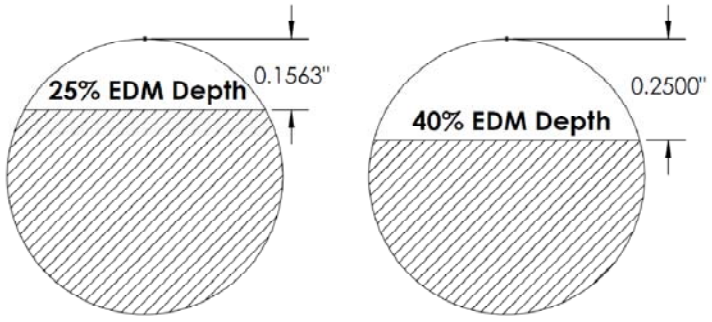

Figure 32 Two shaft cross-sections, wire EDM cut depths.

To create the crack, a machining technique known as wire Electrical Discharge Machining (EDM) is used. This method has been selected due to the high hardness of the material and minimal thickness of the cut made which shall resemble a crack. One limitation of this technique is that the work piece has to be electrically conductive in order to conduct the rapidly recurring spark that erodes the material. Of course, the goal is to create a real crack with zero thickness, but the thinnest wire used for wire EDM has a 0.001" diameter, which makes a 0.0015" wide gap when burn-off from the EDM process is included. The wire used to create the cracks in the shafts is 0.004" in diameter, leaving a 0.0045" wide gap when burn-off is accounted for. A magnified image of the wire EDM cut is shown in Figure 33.

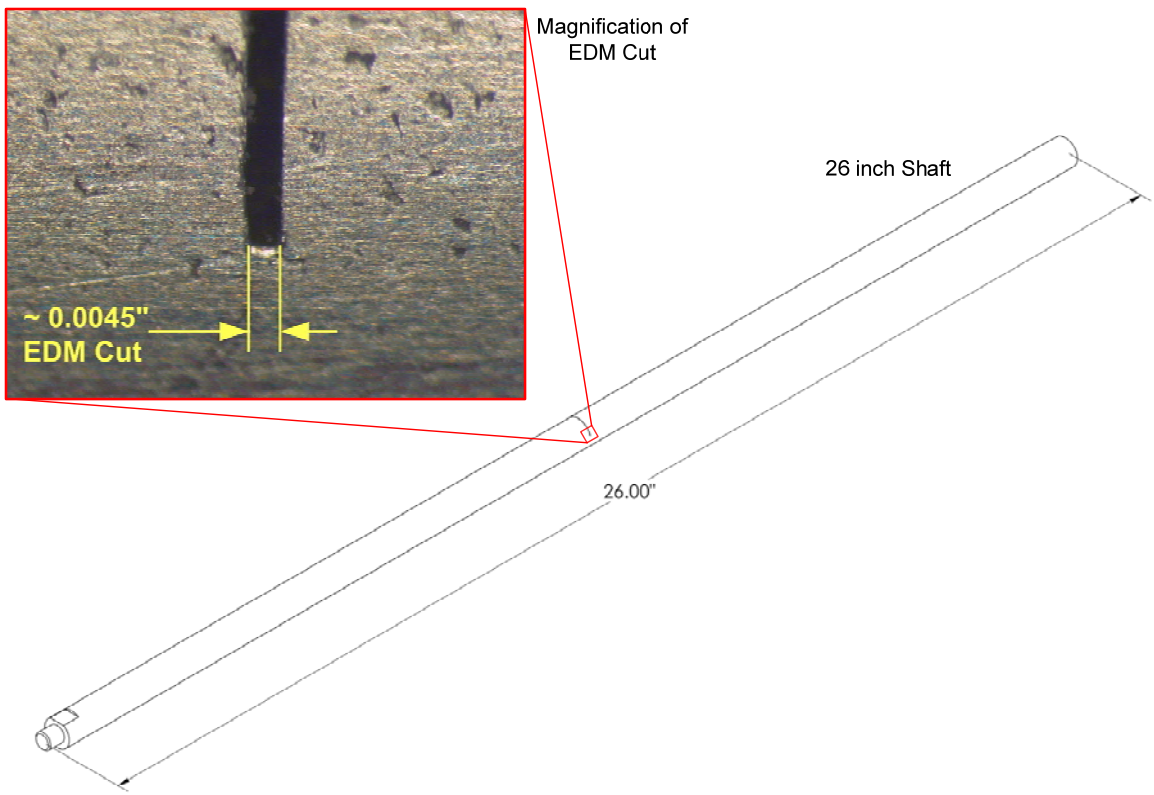

Figure 33 Magnification of EDM cut.

The EDM cut creates a void between the adjacent walls along the cut, while a real crack is a structural separation of a solid material leaving virtually no void. The crack breathing concept assumes that the shaft has zero stiffness reduction when the crack is oriented upwards in the closed position, then, after rotating 180°, the shaft has the maximum stiffness reduction when the crack is oriented downwards in the open position. In the case of a shaft with an EDM cut, when the crack is oriented upwards in the closed position, the shaft will still have reduced stiffness because there is void between the adjacent surfaces of the crack, where the EDM process removed material.

In order to simulate a real crack as closely as possible, the 0.0045” void created by the EDM process is filled with a 316 stainless steel shim. It is expected that this set-up creates a geometric simulation of a crack. As the shaft rotates and the crack turns to the closed position, the void created by the EDM material removal process will be filled tightly with the stainless steel shim. This procedure leads to reducing the amount of void space, which expectantly will provide enough support to furnish a shaft stiffness reduction that approaches zero. To achieve this in practice, the shim that is made of a sheet slightly thicker than the EDM cut, and is sanded in small increments until it tightly fit the EDM cut. Afterwards, final cleanup and sanding is performed to the point where the EDM cut and shim are barely visible to the eye. A magnified image of the shimmed EDM cut is shown in Figure 34.

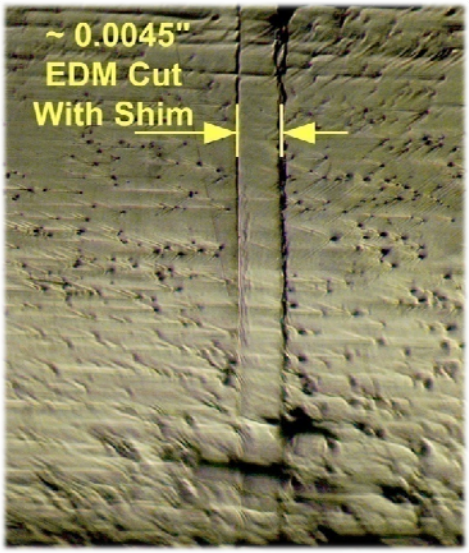

Figure 34 Magnified photo EDM cut in the shaft with shim installed.

The shafts with EDM cut are first tested in an un-shimmed configuration. Upon completion of the un-shimmed configuration testing, the same shafts with EDM cuts are shimmed and then tested again. Comparisons of the data collected between all the shaft configurations are shown in Section 5.2.

The *disk* used for this work is machined from steel and has a 5" diameter and a 1" thickness. This custom made 6.81 lb disk is slightly more than two times heavier than the disk that was originally equipped with Revolve's™ test rig and is used in order to increase the static sag of the rotor. Increasing the sag aids in the weight dominance assumption which helps ensure that the shaft's orbit remains below the bearing centerline for the crack to open and close during shaft rotation. A photo of the 5" disk mounted on the shaft is shown in Appendix A.

The *ball bearings* which support the shaft on both ends are SKF™ ball bearings. They are single row, self adjusting ball bearings with 15 balls per row, featuring a 3.5 mm ball diameter. The self adjustment feature is only intended for minor alignment problems such as if the two bearing mounts are not installed perfectly concentric with each other. For the purpose of modeling, it is essential to make a reasonable estimate of the bearing stiffness which is used in Section 3.5. A general equation for of ball bearing stiffness estimation is shown below.

$$K_R = 1166\cos(\alpha)^{5/3}(IZ)^{2/3}D^{1/3}F_{Bearing}{}^{1/3} \tag{14}$$

In the case of the SKF™ bearing in this test rig, α=0°, $I=1$, $Z=15$, $D=3.5\,\text{mm}$, $F_{Bearing}=28.25\,\text{N}$. The application of this equation yields a bearing stiffness value of $K_R = 32.793\ \text{MN/m}$.

4.2 Data Acquisition

For collection of dynamic data, the ADRE® Sxp software and the 408DSPi (Dynamic Signal Processing Instrument) work together to produce a highly scalable, multi-channel data acquisition system that allows for recording, analyzing, correlating, and diagnosing machines and processes. The system consists of a 408DSPi, ADRE® Sxp client software, and a computer capable of running the software. Its high performance architecture is able to acquire both static and waveform data in parallel at various rates and resolutions. The 408DSPi is a versatile system that incorporates the functionality of many types of instrumentation such as oscilloscopes, spectrum analyzers, filters, signal conditioners, and digital recorders into a single platform. In addition, this system can be operated remotely in network based environments via LAN/WAN to an external computer. The ADRE® Sxp software contains many plotting and data manipulation tools to help analyze and diagnose equipment. The system is capable of producing real-time displays completely independent of data storage to permanent memory [**28**].

For this work, the ADRE® system collects five channels of data; two pairs of probes collect shaft position data and the fifth collects keyphasor data. The Bently-Nevada® 3300 eddy current proximity probes are positioned at horizontal and vertical positions for collection of shaft position data. The same proximity probe is used for all five channels which is shown in Appendix B along with images of the ADRE® 408DSPi unit. All FFT data processing and plotting are done by ADRE® Sxp software, however,

plots are exported out of ADRE® Sxp and re-plotted in MATLAB® due to availability of more flexible plotting options.

For the collection of static data used for system identification, the HP 35670A was utilized. It is a portable two-channel dynamic signal analyzer that has the capability to perform as several instruments at once, which makes it ideal for both R&D and field work. Many of this instrument's features are optimized for troubleshooting mechanical vibration and noise problems, characterizing control systems, or general spectrum and network analysis [**29**]. Images of this instrument are provided in Appendix B.

For this work, an HP 35670A Dynamic Signal Analyzer strictly performed rotor system identification. It was done through the use of an instrumented hammer and accelerometer. An industry standard technique called Experimental Modal Analysis (EMA) is commonly employed which uses an instrumented hammer containing a force transducer to apply a broadband excitation to the test structure and an accelerometer to measure the response of the structure. Both of these components are connected to a frequency analyzer that will output the test structure's transfer function that is calculated via FFT. This is a time-tested, reliable tool which can measure a large span of frequencies of a static structure. Because the accelerometer is directly mounted to the shaft, the rotor must remain static, which means that the system's transfer function will be neglecting gyroscopic effects. After averaging the ten collected FFT trials, a final FFT plot is viewed to identify the natural frequencies of the rotor before operation.

4.3 Signal Injection

The dSPACE™ ControlDesk® software environment combined with dSPACE™ signal management hardware produce a powerful research instrument commonly used in industry for various real-time research applications. This dSPACE™ prototyping system is a research and development tool that is designed to make a significant impact in the development cycle for areas such as automotive engineering, aerospace, and industrial control.

In this work, this system will strictly be used as a means of signal control that is directly coupled to the actuator AMB. This allows for the application of specific signal injections with full control over frequency and magnitude through the use of the dSPACE™ ControlDesk® software environment and a dSPACE™ DS1103 board. This software allows for the creation of a fully customizable graphical user interface to control the parameters under investigation via an interface board. The signal that is sent to the AMB using dSPACE™ is a sine wave with a particular frequency and amplitude. The combination frequency is calculated based on Equation (12) and amplitude is determined experimentally. Further information about AMB signal injection in the experiment is provided in Section 5.2.

4.4 Procedure

Initial steps of planning the work include identifying research goals and how to achieve them at Cleveland State University's test facility. With this in mind, definitions of geometry are defined such as locating the bearings, the crack, the disk, and the actuator

AMB that will best suit the need of this work. Next, two crack depths are chosen as well as three different actuator AMB injection signals for comparison. The selection of actuator AMB injection signals are heavily influenced by simulation and modeling as well as by some preliminary experimental runs. Upon completion of assembling the experimental rotor test rig and the data acquisition system, a test matrix is established. The complete test matrix for this work can be found in Appendix C.

The first step in running experiments with this rotor test rig is to perform system identification. System identification involves using a method to identify some of the rotor's many characteristic properties such as its natural frequencies, its bearing properties, or to extract its damping coefficients. Quite often, this step is in the design process in order to manufacture a rotor that will meet certain criteria.

An accurate way of performing system identification is to slowly run the rotor through its operating range and record its vibration history to a Bode plot to illustrate all the natural frequencies it passes. This is a reliable method because it measures the real system in real operation which includes all possible physical effects. However, often times this is not possible for various reasons, so other methods are used. As mentioned before, commonly used is experimental modal analysis which uses the instrumented hammer coupled with an accelerometer. When this technique is applied to rotors, the rotor has to be idle, which will not account for some dynamic effects. In particular, gyroscopic effects due to disks contribute a stiffening effect that will slightly shift natural frequencies, which in many cases, are insignificant. Another way to identify natural frequencies of a rotor is to perform a sine sweep. This is only common in magnetically levitated systems where there is an AMB present to inject a harmonic force starting with

low frequencies and slowly increasing to finish with high frequencies, meanwhile recording a Bode plot of the sweep. As the injected harmonic forces coincide with the rotor's natural frequencies, the magnitude of vibrations increase which are recorded on the Bode plot. Once again, as in the instrumented hammer system identification technique, the rotor is idle and does not take into account dynamic effects such as the gyroscopic effect.

Once the system identification is complete, the critical speeds are known in order to avoid excessive vibrations at those speeds. Testing with the rotor spinning is done beginning with the healthy shaft, with and without excitation from the actuator AMB. Each shaft will undergo three different harmonic excitation signals from the actuator AMB. Next, the two shafts with un-shimmed cracks are tested with and without excitation from the actuator AMB. Once completed, the two shafts with shimmed cracks are then tested. The testing procedure is repeated from shaft to shaft. Table 2 shows a brief order of shaft testing, arranged in groups. Each group contains four trials due to the four different signal injections where n=2, n=3, and n=4 correspond to signal injection frequencies of 18 Hz, 45 Hz, and 72 Hz, respectively, when applied to Equation (12).

Trial Group	**Shaft Condition**	***n* value**
1	Healthy	none, 2, 3, 4
2	25% Un-shimmed Crack	none, 2, 3, 4
3	40% Un-shimmed Crack	none, 2, 3, 4
4	25% Shimmed Crack	none, 2, 3, 4
5	40% Shimmed Crack	none, 2, 3, 4

Table 2 Brief order of shaft testing

Once data for all groups has been collected, it is processed with the ADRE® Sxp software to produce FFT spectrum plots for all conditions. Once data acquisition and processing is completed, extensive investigation of frequency content for each condition is performed. This allows for comparison of experimental results to simulation and modeling in an effort to establish shaft crack detection criteria. Final conclusions are made.

CHAPTER V

EXPERIMENTAL RESULTS

Experimental data is taken, analyzed, and then compared with simulated data. Initially, system identification is performed through the use of the instrumented hammer to determine the system's transfer function in the non-rotating state following the configuration shown in Figure 27. The results are shown over a large frequency range even though the rotational speed throughout the experiment is 75% of the first critical speed. Since the first critical speed of this rotor is measured and predicted to be approximately 2,160 rpm, the running speed is simply calculated to be 1,620 rpm. The entire experiment is performed at this rotational speed because indications from modeling and simulation in Section 3.5 show that the combination frequency peaks are most clearly shown at this speed.

FFT plots of experimental data are presented using five shaft conditions and four AMB signal injections (shown in blue). Three shafts in total are compared; a healthy

shaft, a shaft with a 25% un-shimmed crack, and a shaft with a 40% un-shimmed crack. Further, the same cracked shafts are tested with shims installed to finally provide five shaft cases with four running trials per shaft.

Simulated FFT data (shown in red) is then compared with experimental data in an effort to find any correlations in frequency content. The finite element model is presented in this chapter along with simulated results and direct comparisons to the experimental data.

5.1 Rotor System Identification

The rotor supported on ball bearings has a measured transfer function shown in Figure 35. This transfer function was measured using the HP 35670A with an instrumented hammer and accelerometer over a 1,600 Hz frequency range. Each peak on the plot represents a natural frequency of the rotor system in the non-rotating state. It is important to note that these measured peaks will not exactly match the rotor's critical speeds in its rotating state due to the lack of the gyroscopic effect which acts as a stiffener in the system. The important feature of this plot is the first natural frequency which is required for setting the running speed to be 75% of the rotor's first critical speed.

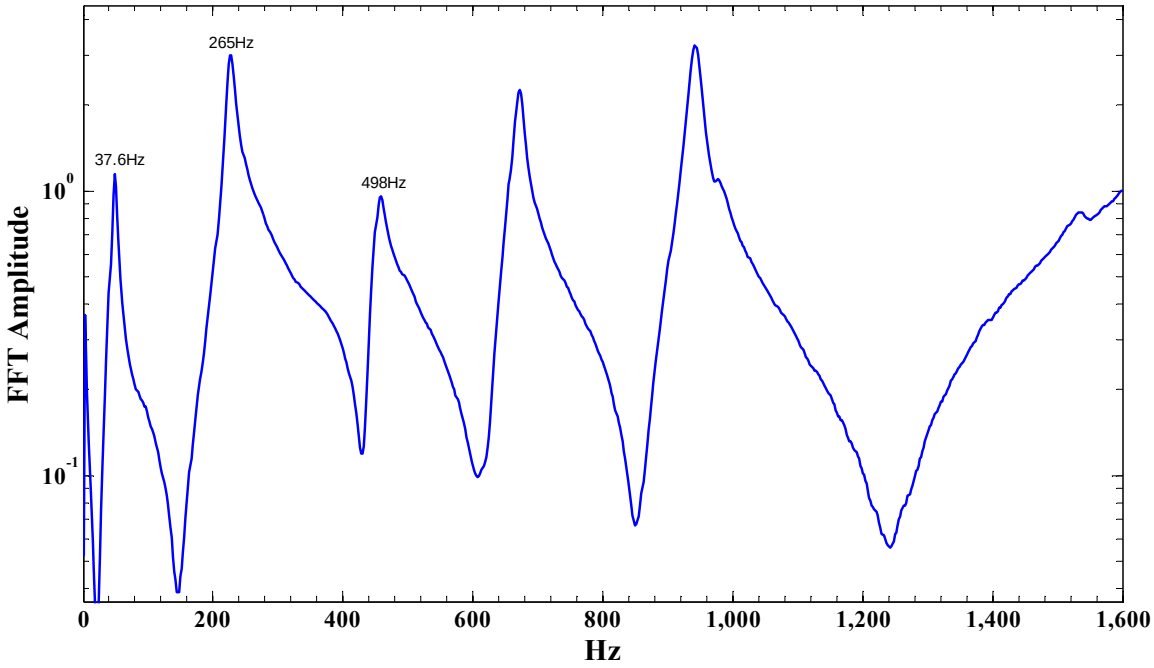

Figure 35 Measured transfer function of the un-cracked rotor via an instrumented hammer.

The simulated data in this thesis is obtained using the finite element model shown in Figure 36 which consists of 28 elements and 29 nodes, with dimensions that are consistent with the test hardware in Figure 27. Ball bearing supports are modeled at nodes 2 and 27 and the actuator AMB force injection is modeled at node 13. Ball bearing stiffness is roughly calculated to be 32.793 MN⁄m in all radial directions derived from Equation (14) with damping values assumed to be 10 N·s⁄m. For all signal injection trials, the actuator AMB force is estimated to be 10 N which is calculated from Equation (13) and experimentally verified. A detailed finite element model of the rotor is dimensioned in Appendix A. The rotor has a modeled unbalance of 0.001 kg·m located at node 17 and is composed of material properties for average stainless steel which are as

follows; E = 206.8 GPa, ν = 0.3, G = 82.7 GPa, and ρ = 7888.7 kg/m^3 . The shaft crack is modeled at the 16th element.

This simulation is plotted over a span of 20,000 rpm (333 Hz) which shows the first two critical speeds of the test rig. This is done to show that the model closely simulates the real system. Figure 37 shows simulations of the unbalance response on the left side and the Campbell diagram on the right side. The important feature in this figure is that the simulated first critical speed of 2,160 rpm (36 Hz) closely matches the measured first natural frequency in Figure 35 of 37.6 Hz. This finite element model closely models the real system and will be used further in Section 5.3.

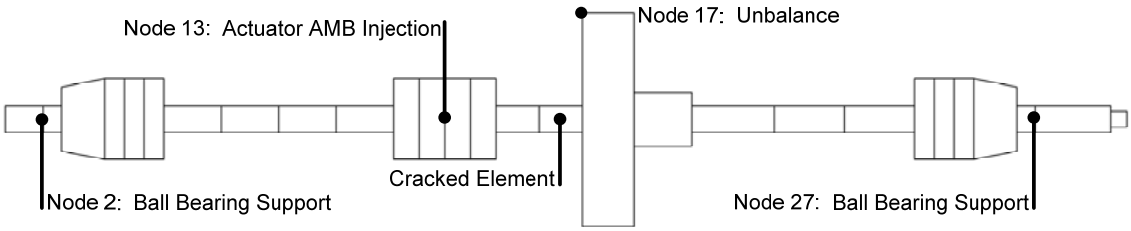

Figure 36 Finite element model used for simulations.

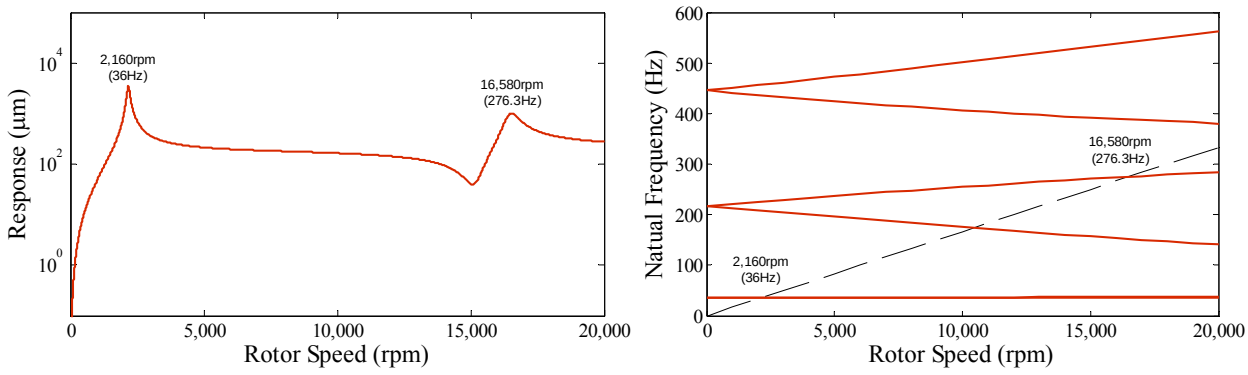

Figure 37 *Left:* Unbalance response simulation. *Right:* Campbell diagram.

For visualization of the first two flexible mode shapes, Figure 38 illustrates the simulated orbit path at each node of the finite element model calculated at 10,000 rpm. Although 1,620 rpm is not quite the first critical speed, it can be assumed that orbiting shape of the shaft is approximately what is pictured in the left image of the figure.

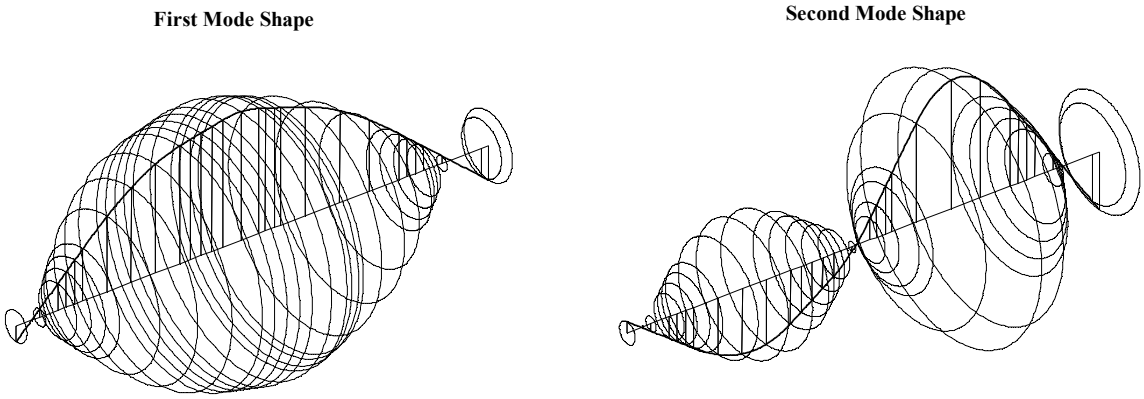

Figure 38 First two flexible mode shapes at 10,000 rpm

5.2 Experimental Data

The experimental data follows a format that is repeated for all experimental figures shown and follows the hardware configuration illustrated in Figure 27. Four FFT plots are shown in each figure starting with the spinning rotor with no signal injection, followed by three FFT plots of the spinning rotor with signal injections of n=2 (18 Hz), n=3 (45 Hz), and n=4 (72 Hz). These injection frequencies are calculated following Equation (12) for the reason that they span over a relatively large range around the running speed of 1,620 rpm (27 Hz). The force injection magnitude from the actuator AMB for each injection frequency is chosen to be roughly 75% to 85% of the magnitude required to force the shaft into rubbing with the actuator AMB backup bearing which was

found experimentally. This AMB force is approximately calculated in Section 4.1.1 which is necessary to model the system in Section 3.3.

Combination frequencies correspond to the result of all n values when applied to Equation (12). This equation requires ω_n and Ω which are 36 Hz and 27 Hz, respectively, in the experimental cases for this thesis. In addition to obtaining the AMB signal injection frequency, in this case the *n value* can be varied from -4 to 6 in integer increments to calculate all the combination frequencies within the 150 Hz span that all the FFT figures are plotted with. These frequencies appear in the FFT spectrums which are of primary interest in this work. On the FFT plots, these frequencies are labeled in *italic* style. Table 3 shows calculated combination frequencies which may be present in the FFT spectrum plots.

***n* value**	**Ω (Hz)**	**ω_n (Hz)**	**Ω_{AMB} / Combination Frequency (Hz)**
-4	27	36	144
-3	27	36	117
-2	27	36	90
-1	27	36	63
0	27	36	36
1	27	36	9
2	**27**	**36**	**18**
3	**27**	**36**	**45**
4	**27**	**36**	**72**
5	27	36	99
6	27	36	126

Table 3 Combination frequencies for corresponding *n* values.

It should be noted that all plots are illustrated with a log scale in the vertical axis. This is done to amplify the visual effect of frequencies with weaker amplitudes that

would otherwise not be seen on a linear scale. An arbitrarily chosen example of this is shown in Figure 39 where the same FFT plot of the healthy shaft's response is shown in both a linear scale and a logarithmic scale. Using the linear scale, it is obvious that the 1X component is clearly dominant compared to the natural frequency and multiples of the running speed. However, in order to observe more subtle frequency content, a logarithmic scale is used.

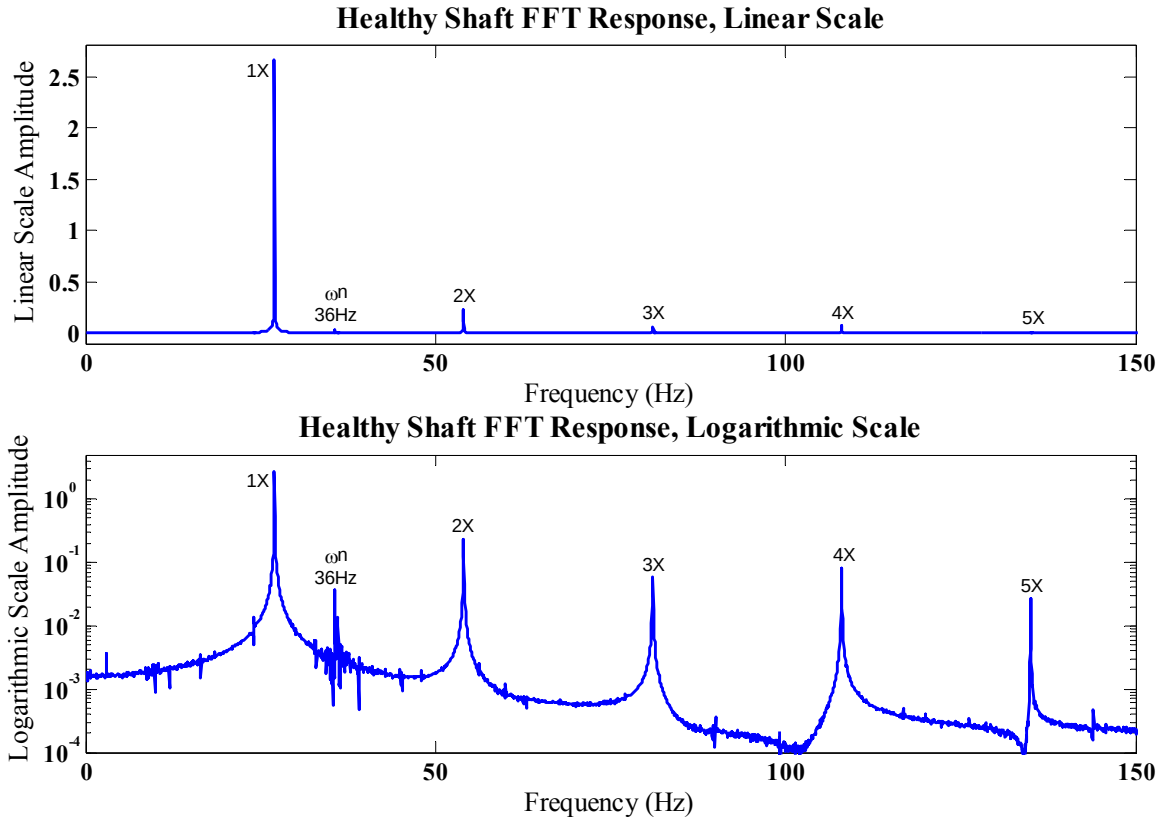

Figure 39 Healthy shaft FFT plot comparison of linear vs. logarithmic scale.

5.2.1 Un-cracked Shaft Data

The first shaft tested is the healthy, un-cracked shaft. The rotor speed is set to 2,160 rpm and stays consistent throughout the experiment as well as the configuration. Four FFT plots are presented in a vertical array so they can be visually compared. AMB signal injection frequency is the only parameter varied and is labeled per plot. For the healthy shaft case only, FFT data is shown for both the horizontal proximity probe in Figure 40 and the vertical proximity probe in Figure 41.

Features consistent with all four FFT plots are discussed. Commonly, the dominant frequency of the FFT spectrum is the running speed of 27 Hz (1,620 rpm), known as the 1X component, and is present in any rotating system due to residual unbalance. Directly linked to the 1X component are its multiples of 2X, 3X, 4X, and 5X with much smaller amplitudes which are generally caused by nonlinearities in the system (every system is nonlinear) and imperfections. Following the running speed, the rotor's first critical speed emerges as a noisy peak located at 36 Hz, which is always excited to some extent.

The first trial shows FFT data of the spinning rotor without AMB excitation. The result shows no combination frequency content. The trials with AMB excitation are plotted in the last three plots of the figures and have features unique to each of them. AMB signal injections appear as peaks in the FFT spectrum at the corresponding frequencies which are labeled on the plots. The second plot of the figure has an AMB injection peak at 18 Hz, the third plot has an AMB injection peak at 45 Hz, and the fourth plot has an AMB injection peak at 72 Hz. The plots with AMB signal injections begin to

show traces of combination frequencies peaks emerging (labeled in *italics*), but their amplitudes are negligible.

Figure 40 and Figure 41 are shown to illustrate the slight difference in the data with respect to the horizontal and vertical proximity probes. The data taken with the vertical proximity probes have slightly larger vibration amplitudes and more evident combination frequency content than data taken with the horizontal proximity probes. In addition, the AMB signal injection frequency peaks are much more evident in the data recorded with the vertical proximity probes. This can be expected because the actuator AMB forces the shaft to vibrate vertically which coincides with the vertical proximity probe orientation. So as a result, the FFT spectrum recorded in the vertical direction has stronger vibration responses than in the horizontal direction. In an effort to best visualize the frequency content in the FFT spectrums, only data recorded with the vertical proximity probe is presented in the remaining four experimental cases.

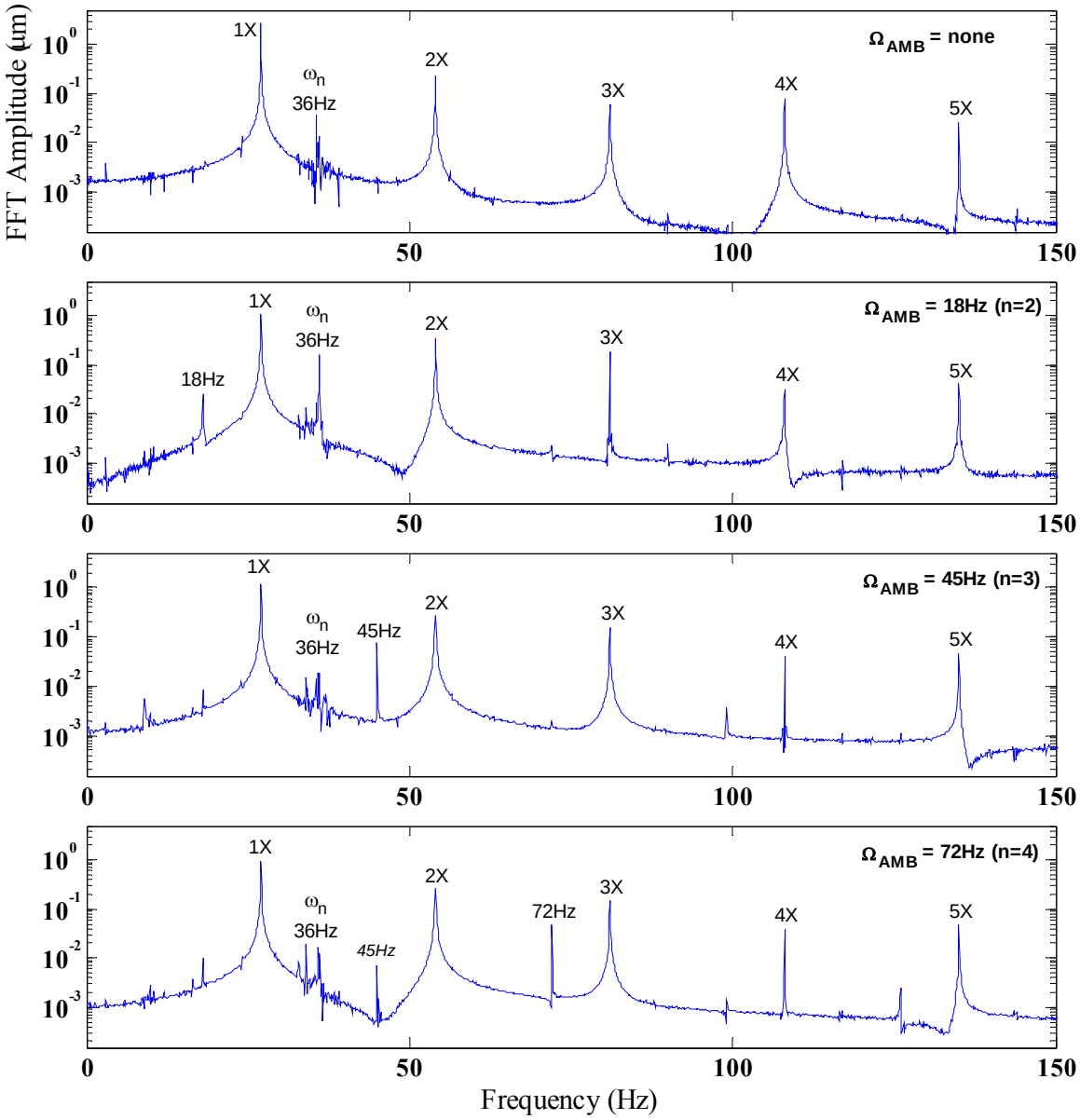

Figure 40 Horizontal proximity probe responses for the healthy rotor. Ω=27 Hz, external force of 10 N with various frequencies.

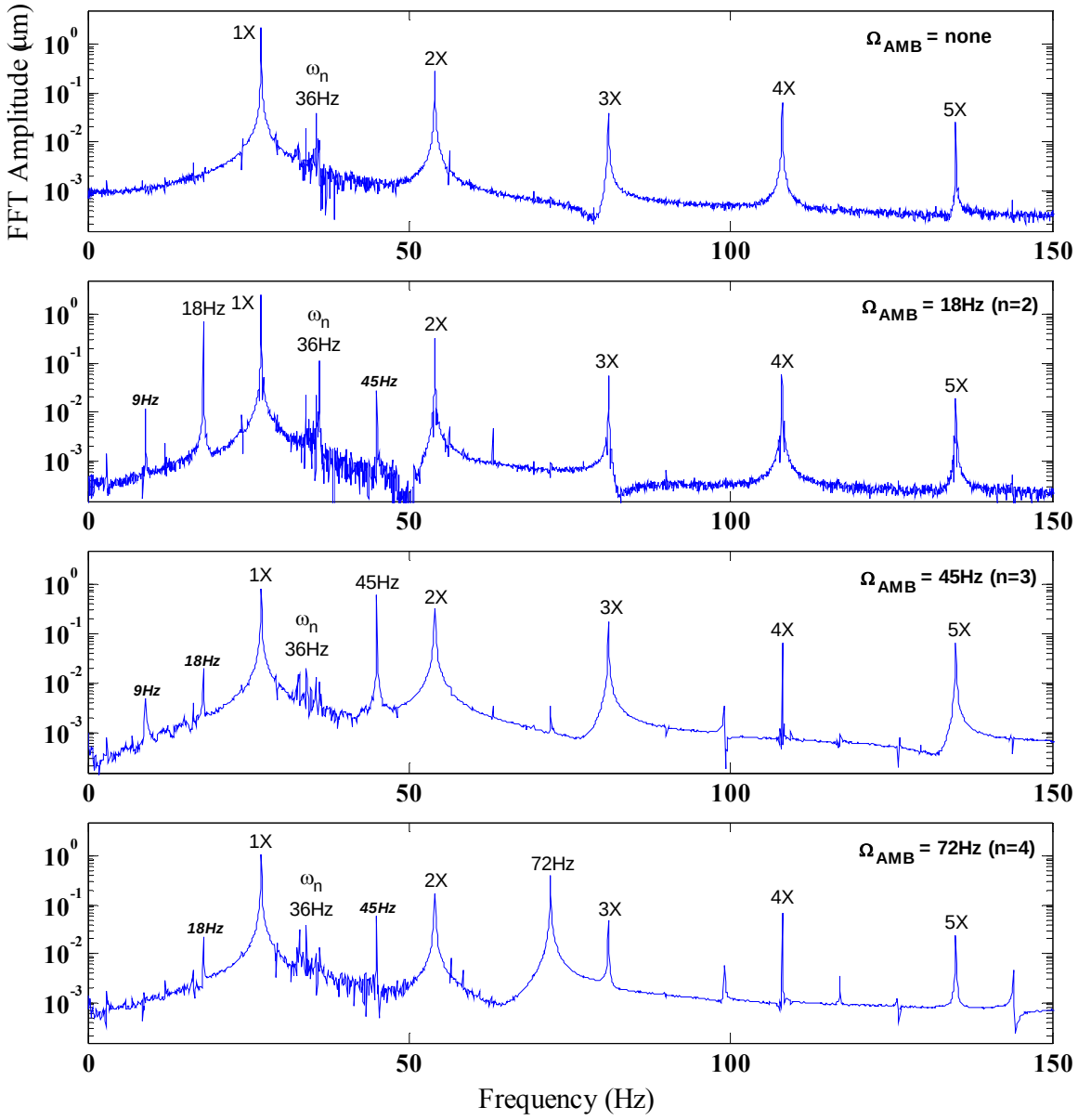

Figure 41 Vertical proximity probe responses for the healthy rotor. Ω=27 Hz, external force of 10 N with various frequencies.

5.2.2 Shaft with 25% Un-shimmed Crack Data

The set of trials shown in Figure 42 use the shaft with an un-shimmed crack 25% of the shaft diameter. All parameters such as running speed and magnetic actuator force excitation frequencies are repeated from the previous case.

Features consistent with all four FFT plots are consistent with previous trials. The dominant frequency of the FFT spectrum is the running speed of 27 Hz (1,620 rpm) or 1X. Directly linked to the 1X component are its multiples of 2X, 3X, 4X, and 5X. Following the 1X component, the rotor's first critical speed emerges as a noisy peak located at 36 Hz.

The first trial shows FFT data of the spinning rotor without AMB excitation which results in no combination frequency content. The trials with AMB excitation are plotted in the last three plots of the figure. AMB force injections appear as peaks in the FFT spectrum at the corresponding frequencies. The second plot of the figure has an AMB injection peak at 18 Hz, the third plot has an AMB injection peak at 45 Hz, and the fourth plot has an AMB injection peak at 72 Hz.

The three plots with AMB force injections show a significant difference in combination frequency content and amplitudes in comparison with the healthy shaft case. It is evident that combination frequency peaks (shown in *italics*) are more common as well as appear larger in amplitude, due to the presence of the 25% crack. Also, the magnitudes of the responses at the induced combinational frequencies are larger for higher excitation frequencies.

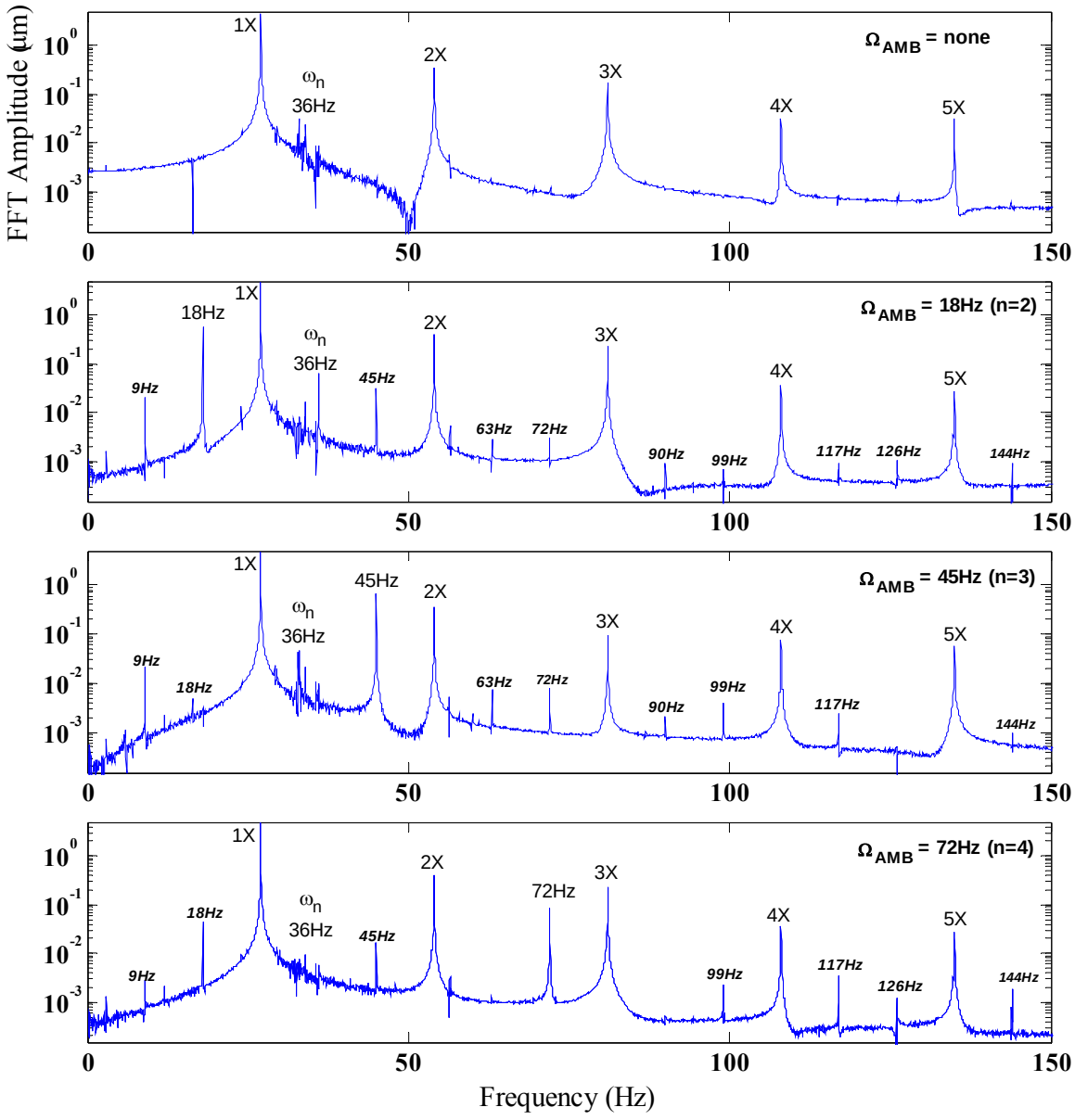

Figure 42 Responses for the rotor with 25% un-shimmed crack. Ω=27 Hz, external force of 10 N with various frequencies.

5.2.3 Shaft with 40% Un-shimmed Crack Data

The set of trials shown in Figure 43 use the shaft with an un-shimmed crack 40% of the shaft diameter. All parameters such as running speed and magnetic actuator force excitation frequencies are repeated from previous cases.

Features consistent with all four FFT plots are consistent with previous trials. The dominant frequency of the FFT spectrum is the running speed of 27 Hz (1,620 rpm) or 1X. Directly linked to the 1X component are its multiples of 2X, 3X, 4X, and 5X. Following the 1X component, the rotor's first critical speed emerges as a noisy peak located at 36 Hz.

The first trial shows FFT data of the spinning rotor without AMB excitation which results in no combination frequency content. The trials with AMB excitation are plotted in the last three plots of the figure. AMB force injections appear as peaks in the FFT spectrum at the corresponding frequencies which are labeled. The second plot of the figure has an AMB injection peak at 18 Hz, the third plot has an AMB injection peak at 45 Hz, and the fourth plot has an AMB injection peak at 72 Hz.

The three plots with AMB force injections show a significant difference in frequency content and amplitudes in comparison with the healthy shaft case. In addition, the FFT results show similar combination frequency content but with an increasing trend in amplitude when compared to the 25% cracked shaft. The three plots with AMB injection essentially contain all the combination frequencies listed in Table 3. Also, the magnitudes of the responses at the induced combinational frequencies are larger for higher excitation frequencies.

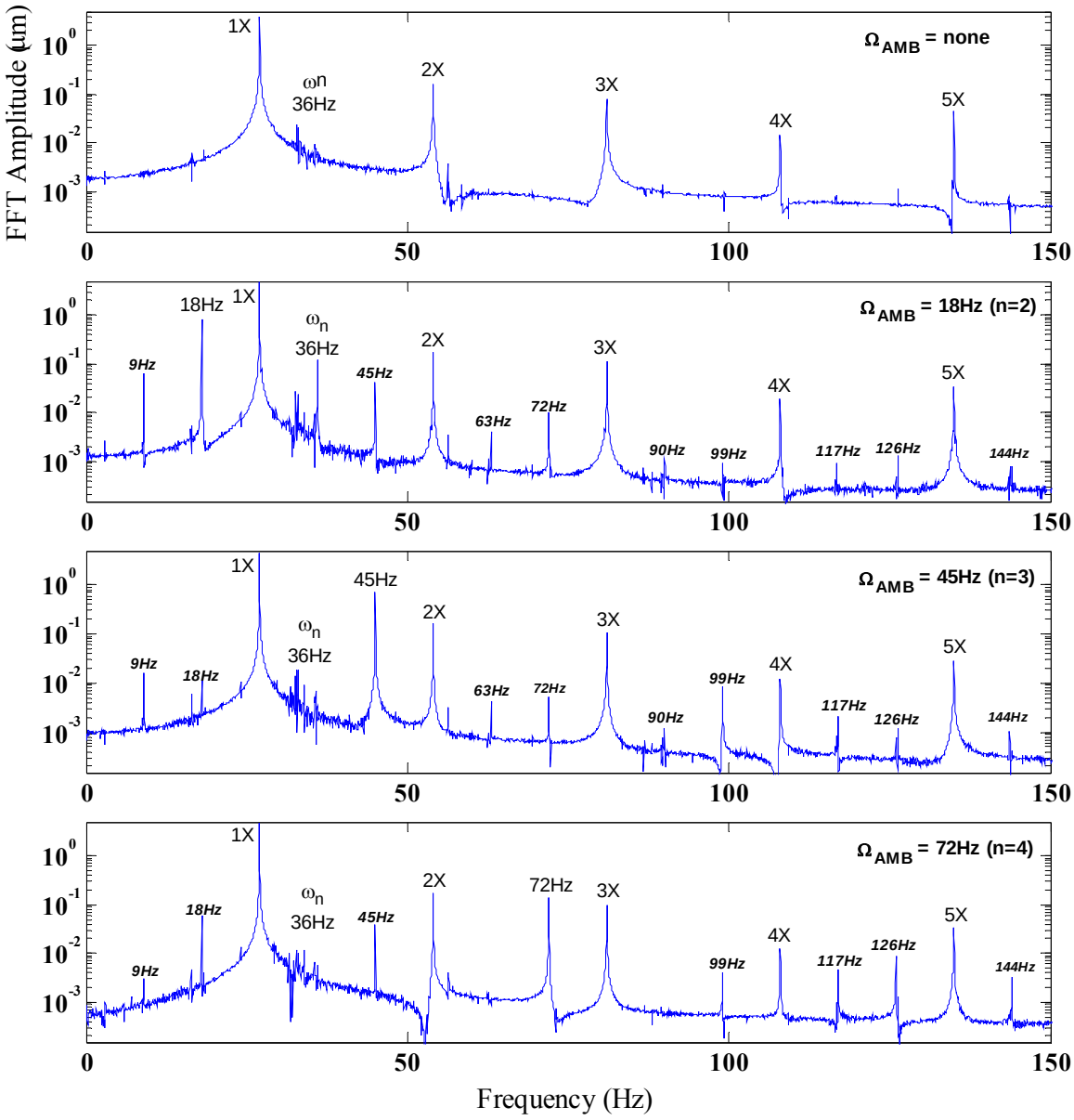

Figure 43 Responses for the rotor with 40% un-shimmed crack. Ω=27 Hz, external force of 10 N with various frequencies.

5.2.4 Shaft with 25% Shimmed Crack

The set of trials shown in Figure 44 uses the shaft with a shimmed crack 25% of the shaft diameter. As described in Section 4.1.2, the void created by the wire EDM process is filled with a metal shim in an effort to more closely simulate a real crack. All parameters such as running speed and magnetic actuator force excitation frequencies are repeated from the previous cases.

Features consistent with all four FFT plots are consistent with previous trials. The dominant frequency of the FFT spectrum is the running speed of 27 Hz (1,620 rpm) or 1X. Directly linked to the 1X component are its multiples of 2X, 3X, 4X, and 5X. Following the 1X component, the rotor's first critical speed emerges as a noisy peak located at 36 Hz.

The first trial shows FFT data of the spinning rotor without AMB excitation which results in no combination frequency content. The trials with AMB excitation are plotted in the last three plots of the figure. AMB force injections appear as peaks in the FFT spectrum at the corresponding frequencies. The second plot of the figure has an AMB injection peak at 18 Hz, the third plot has an AMB injection peak at 45 Hz, and the fourth plot has an AMB injection peak at 72 Hz.

This shaft with the shimmed crack exhibits very similar FFT spectrums as the un-shimmed shaft. The combination frequency content and amplitudes are marginally more defined in this case than the FFT spectrums in the 25% un-shimmed case. This indicates that attempting to mimic a crack more closely by installing shims may not make a significant difference.

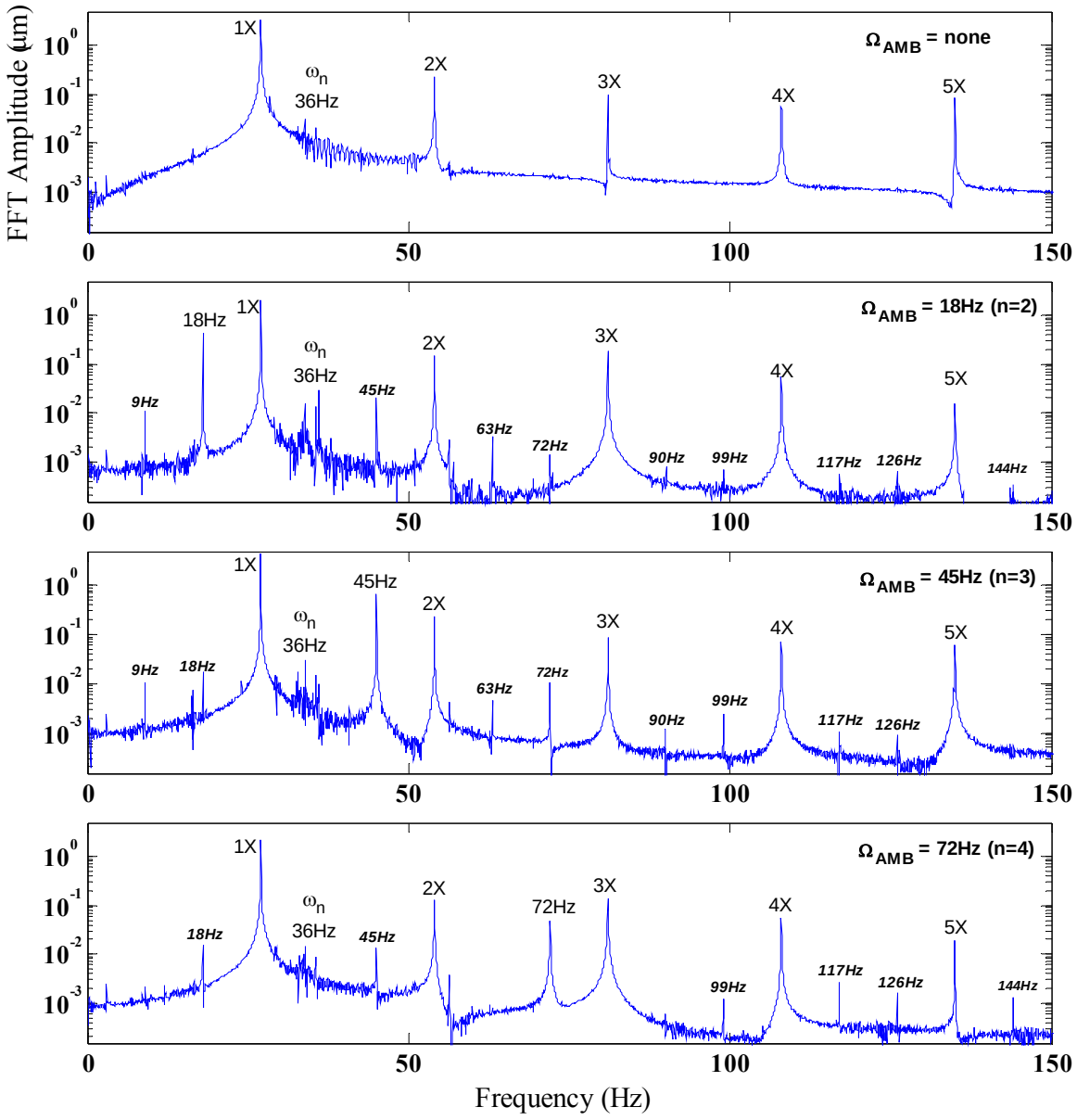

Figure 44 Responses for the rotor with 25% shimmed crack. Ω=27 Hz, external force of 10 N with various frequencies.

5.2.5 Shaft with 40% Shimmed Crack

The set of trials shown in Figure 45 uses the shaft with a shimmed crack 40% of the shaft diameter. As described in Section 4.1.2, the void created by the wire EDM machining process is filled with a metal shim in an effort to more closely simulate a real crack. All parameters such as running speed and magnetic actuator force excitation frequencies are repeated from the previous cases.

Features consistent with all four FFT plots are consistent with previous trials. The dominant frequency of the FFT spectrum is the running speed of 27 Hz (1,620 rpm) or 1X. Directly linked to the 1X component are its multiples of 2X, 3X, 4X, and 5X. Following the 1X component, the rotor's first critical speed emerges as a noisy peak located at 36 Hz.

The trials with AMB excitation are plotted in the last three plots of the figure. AMB signal injections appear as peaks in the FFT spectrum at the corresponding frequencies which are labeled. The second plot of the figure has an AMB injection peak at 18 Hz, the third plot has an AMB injection peak at 45 Hz, and the fourth plot has an AMB injection peak at 72 Hz.

The three plots with AMB force injections are showing a significant difference in frequency content and amplitudes in comparison with the healthy shaft case. In addition, the FFT results show similar frequency content but with an increasing trend in amplitude when compared to the 25% shimmed cracked shaft. This shaft with the shimmed crack exhibits very similar FFT spectrums as the 40% un-shimmed shaft. The combination frequency content and amplitudes are marginally more defined in this case than the FFT

spectrums in the 40% un-shimmed case. This, like the shimmed 25% case, indicates that attempting to mimic a crack more closely by installing shims may not make a significant difference.

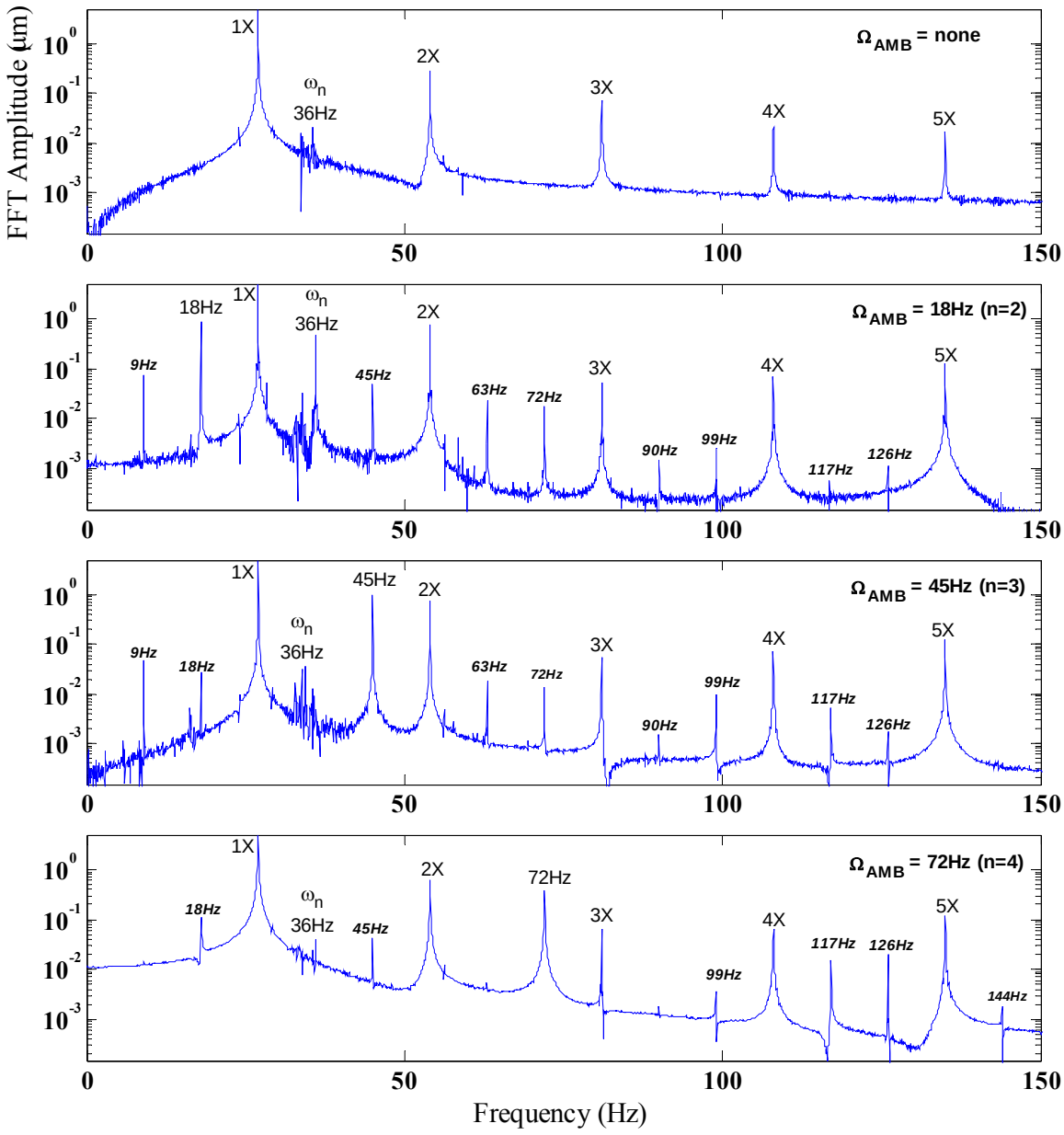

Figure 45 Responses for the rotor with 40% shimmed crack. Ω=27 Hz, external force of 10 N with various frequencies.

5.2.6 Experimental Modal Analysis

In addition to the FFT spectrum results presented in the previous sections, Figure 46 illustrates a comparison of two FFT spectrums of a non-rotating rotor. This was experimentally acquired through the use of the HP 35670A Dynamic Signal Analyzer with the instrumented hammer and accelerometer. Since this thesis concentrates on the data of a rotating rotor and a breathing crack, only one data set is presented below.

Shown with the solid and dotted lines are the FFT results for the rotor with no crack and for the rotor with a 40% crack, respectively. Modes one, two, and four are for both un-cracked and damaged shafts are in the same locations on the frequency axis. However, the key features of this comparison are the locations of modes three and five. The damaged shaft shows a 27 Hz shift to the left at the third mode and a 54 Hz shift to the left at the fifth mode. The FFT amplitudes of the shaft with 40% crack are generally higher than the healthy shaft's FFT amplitudes which can be expected due to the slight reduction of shaft stiffness. This result agrees with work done by Bash [**21**].

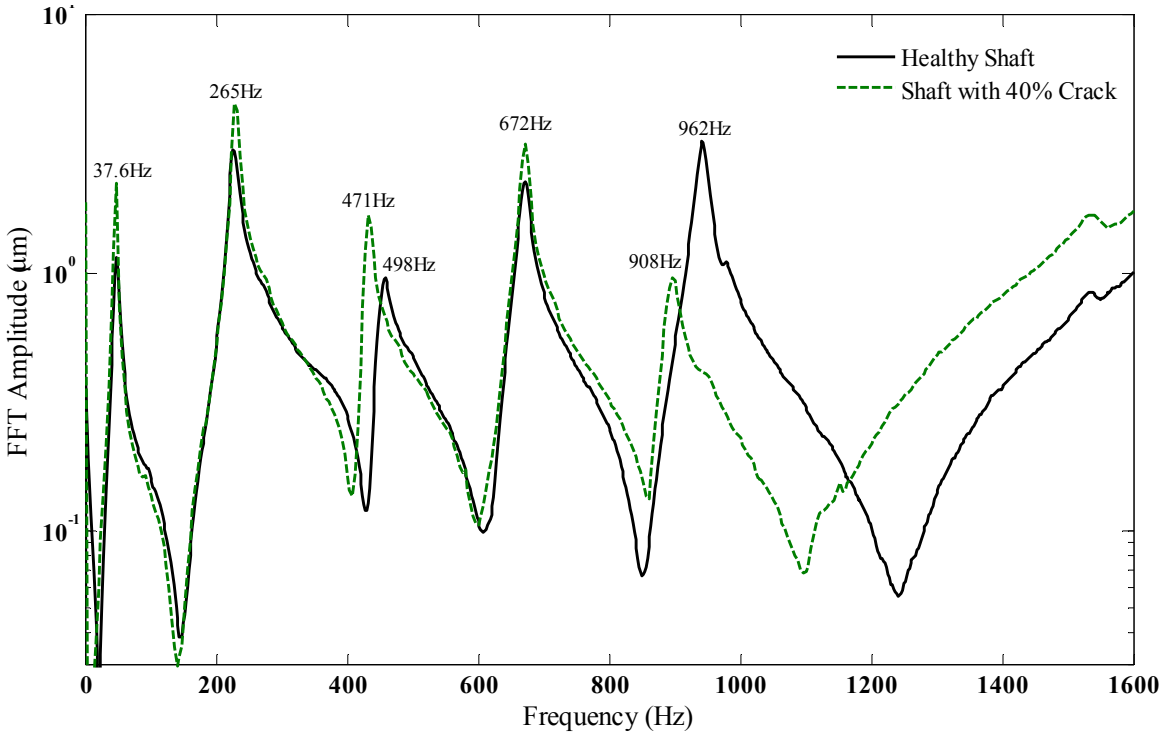

Figure 46 Measured FFT comparison of the healthy vs. the shaft with a 40% crack.

5.3 Comparison of Experimental and Simulated Data

Utilizing the finite element model shown in Figure 36 and following the crack modeling method described in Section 3.3, the results are presented in same format as the experimental data in the previous sections. The following rotor dynamic simulations present ideal cases which neglect effects from rotor imperfections and nonlinearities in the system which provide clean spectral plots.

5.3.1 Healthy, Un-cracked Shaft Simulation

The set of simulation trials shown in Figure 47 use the healthy, un-cracked shaft model. All parameters such as running speed and actuator AMB signal injection frequencies are consistent with previous cases.

The common features of the simulated trials are discussed. The dominant frequency of the FFT spectrum is the running speed of 27 Hz (1,620 rpm) or 1X. However, since the simulations assume the ideal case, imperfections and nonlinearities in the system are nonexistent, producing no multiples of the running speed or any excitation of the shaft's natural frequency. Because of this, the FFT spectrums of the healthy shaft contain only the rotational frequency and the AMB signal injection frequency.

The first trial shows the simulation's FFT spectrum containing only the running speed. This is an idealized simulation which produced is a very narrow and distinct peak. In the last three simulation trials with AMB signal injection, clear peaks emerge at the corresponding frequencies. The second plot of the figure has an AMB injection peak at 18 Hz, the third plot has an AMB injection peak at 45 Hz, and the fourth plot has an AMB injection peak at 72 Hz.

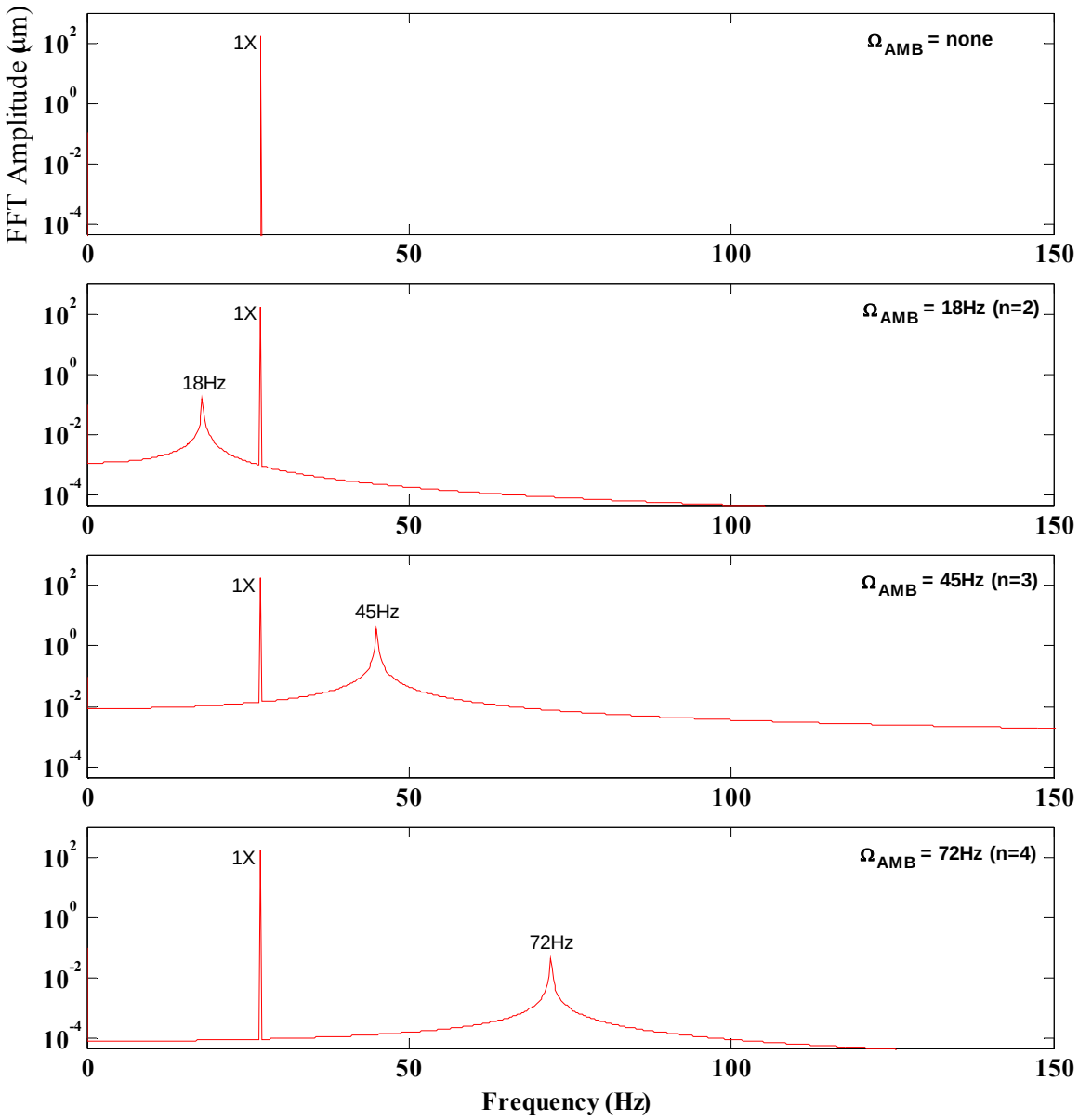

Figure 47 Simulated responses for the healthy rotor. Ω=27 Hz, external force of 10 N with various frequencies.

5.3.2 Simulation of Shaft with 25% Crack

The set of simulation trials shown in Figure 47 use the 25% cracked shaft model. All parameters such as running speed and magnetic actuator force excitation frequencies are consistent with previous cases.

The common features of the simulated trials are discussed. The dominant frequency of the FFT spectrum is the running speed of 27 Hz (1,620 rpm) or 1X. With the crack introduced in the simulation, multiples of the running speeds materialize as 2X, 3X, and 4X on the FFT spectrum plots.

In the last three simulation trials with AMB force injection, clear peaks emerge at the corresponding AMB injection frequencies. The second plot of the figure has an AMB injection peak at 18 Hz, the third plot has an AMB injection peak at 45 Hz, and the fourth plot has an AMB injection peak at 72 Hz.

Combination frequencies appear due to the presence of the crack when AMB force injection is applied. These frequencies are labeled in *italics* on the plots and directly correspond to the combination frequencies listed in Table 3. There is a clear difference in frequency content between the healthy shaft simulation and this case.

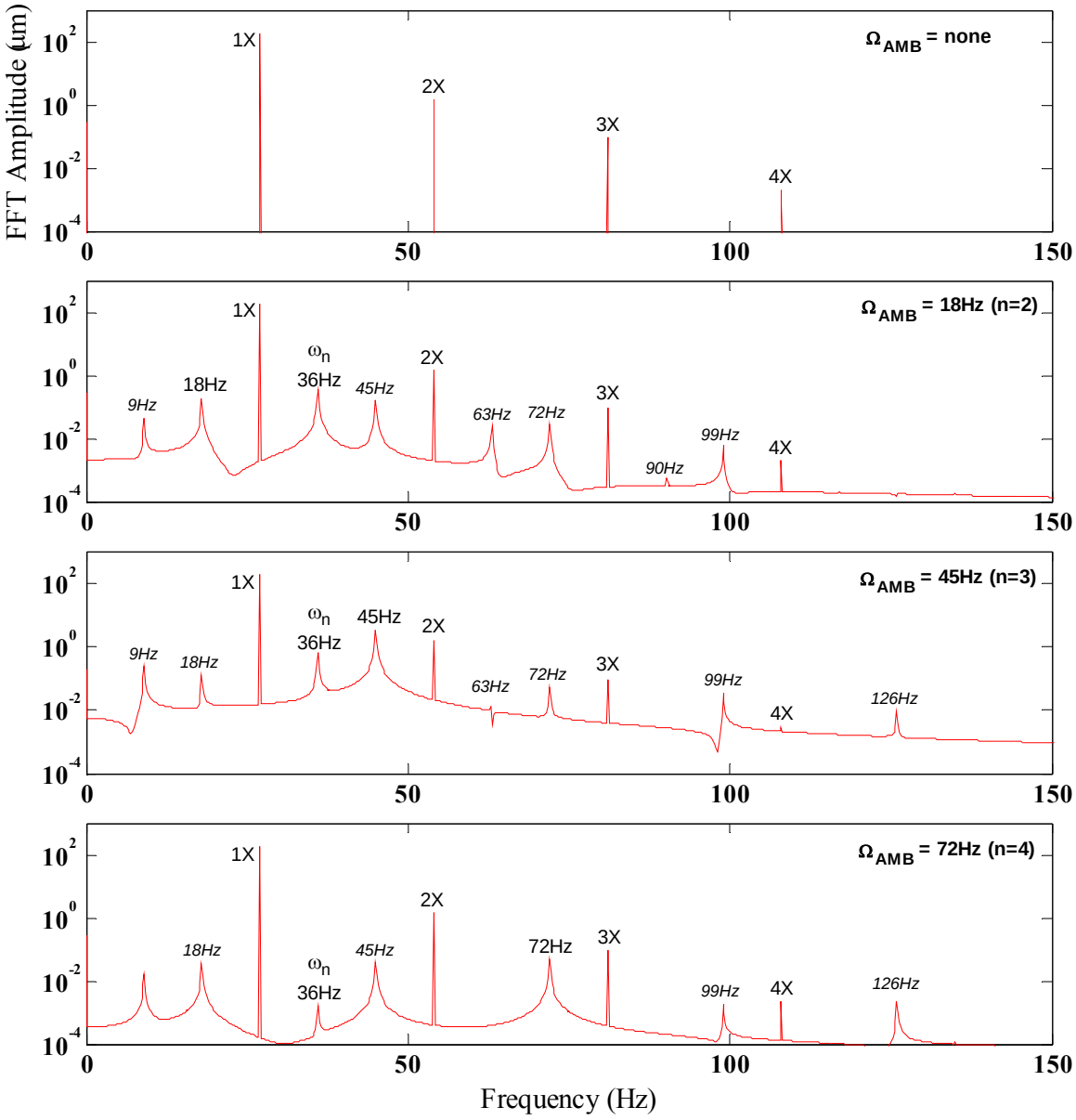

Figure 48 Simulated responses for the rotor with a 25% crack. Ω=27 Hz, external force of 10 N with various frequencies.

5.3.3 Simulation of Shaft with 40% Crack

The set of simulation trials shown in Figure 49 use the 40% cracked shaft model. All parameters such as running speed and magnetic actuator force excitation frequencies are consistent with previous cases.

The common features of the simulated trials are discussed. The dominant frequency of the FFT spectrum is the running speed of 27 Hz (1,620 rpm) or 1X. With the crack introduced in the simulation, multiples of the running speeds materialize as 2X, 3X, and 4X on the FFT spectrum plots.

In the last three simulation trials with AMB force injection, clear peaks emerge at the corresponding AMB injection frequencies. The second plot of the figure has an AMB injection peak at 18 Hz, the third plot has an AMB injection peak at 45 Hz, and the fourth plot has an AMB injection peak at 72 Hz.

Combination frequencies appear due to the presence of the crack when AMB force injection is applied. These frequencies are labeled in *italics* on the plots and directly correspond to the combination frequencies listed in Table 3. There is a clear difference in frequency content between the healthy shaft simulation and this case. In addition, there is a slight increase in amplitude of the 40% shaft crack simulation in comparison with the 25% shaft crack simulation. With the increase in crack depth, the 5X component emerges and as well as traces of a few additional combination frequencies.

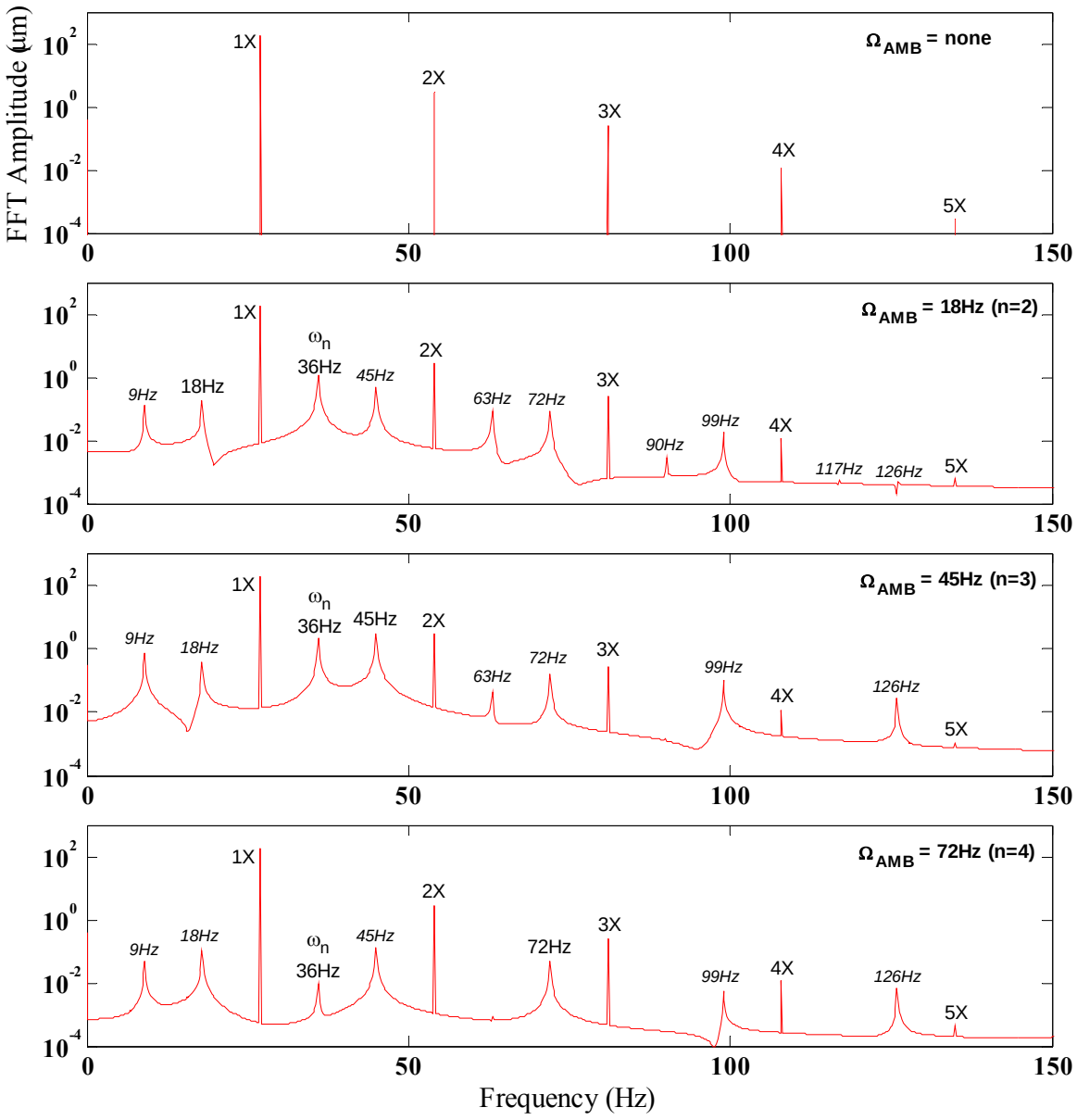

Figure 49 Simulated responses for the rotor with a 40% crack. Ω=27 Hz, external force of 10 N with various frequencies.

5.3.4 Comparison of Simulation and Experiment

A direct comparison of simulation and experimental data is presented in Figure 50, Figure 51, and Figure 52. These comparisons use the 40% cracked shaft with magnetic actuator force excitation frequencies of 18 Hz, 45 Hz, and 72 Hz shown in the corresponding plots. Each plot contains equivalent parameters between the simulation and experiment that have been used through this thesis.

It is clearly visible that the simulation closely resembles the experimental data in the FFT spectrums. The frequency content matches very well, specifically, the running speed and its multiples, AMB force injection, natural frequency, and combination frequencies. The simulation however, shows FFT amplitudes that are much higher and more clearly defined than in the experimental data. Even though the simulation presents an idealistic scenario and shows higher amplitudes and cleaner responses, the experimental data agrees very well.

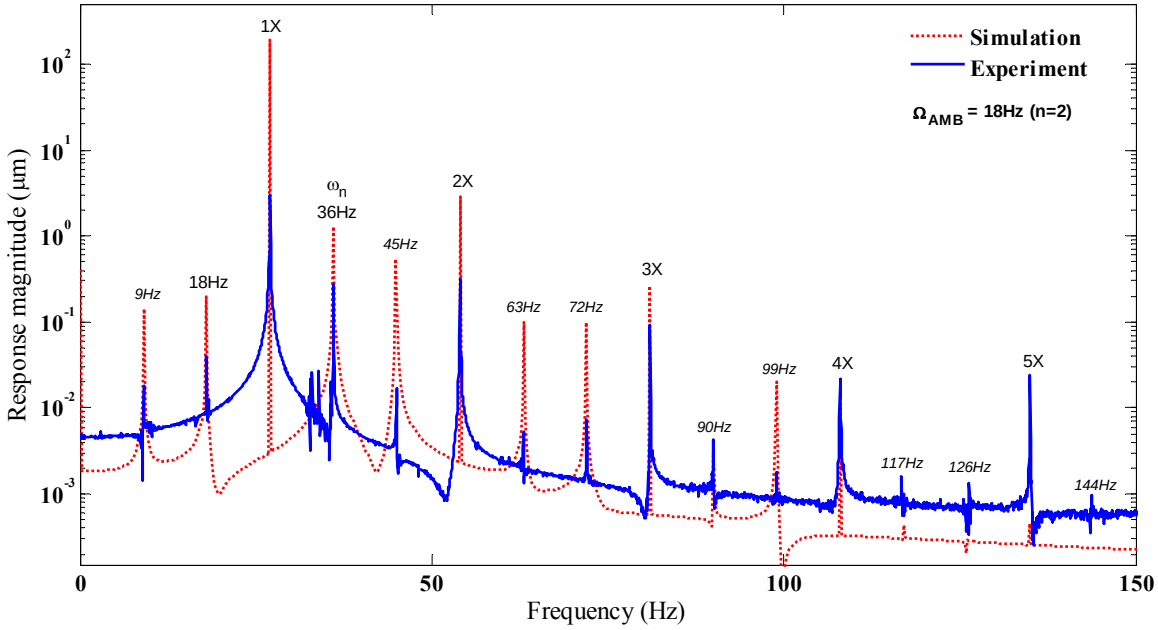

Figure 50 Comparison between simulation and experimental data, 40% cracked rotor. Ω=27 Hz and external force of 10 N.

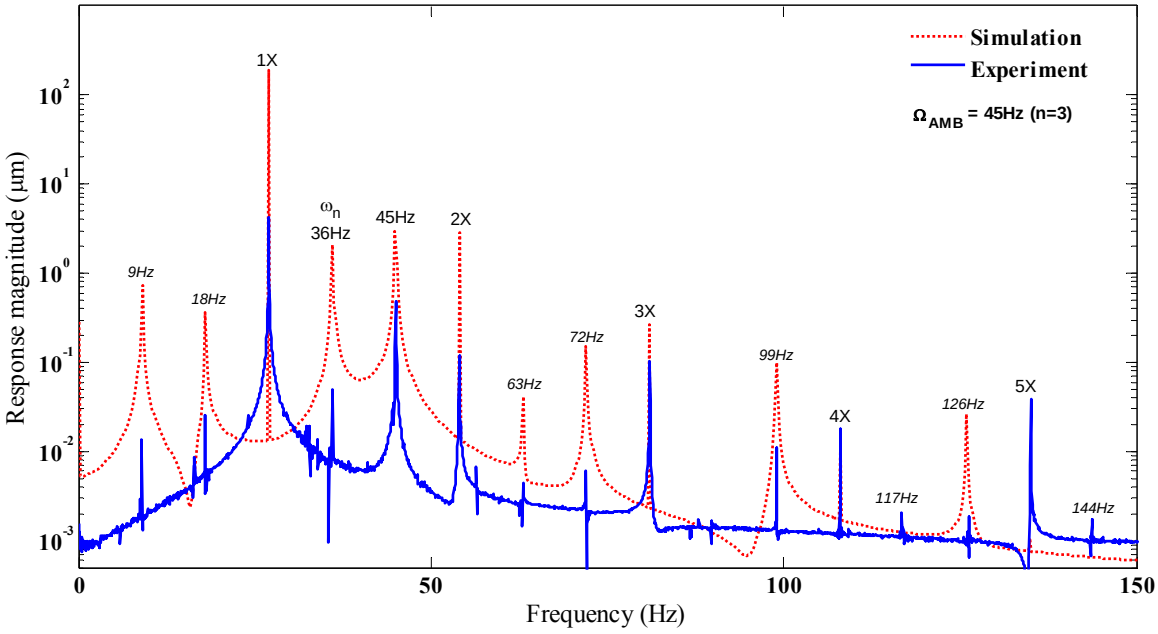

Figure 51 Comparison between simulation and experimental data, 40% cracked rotor. Ω=27 Hz and external force of 10 N.

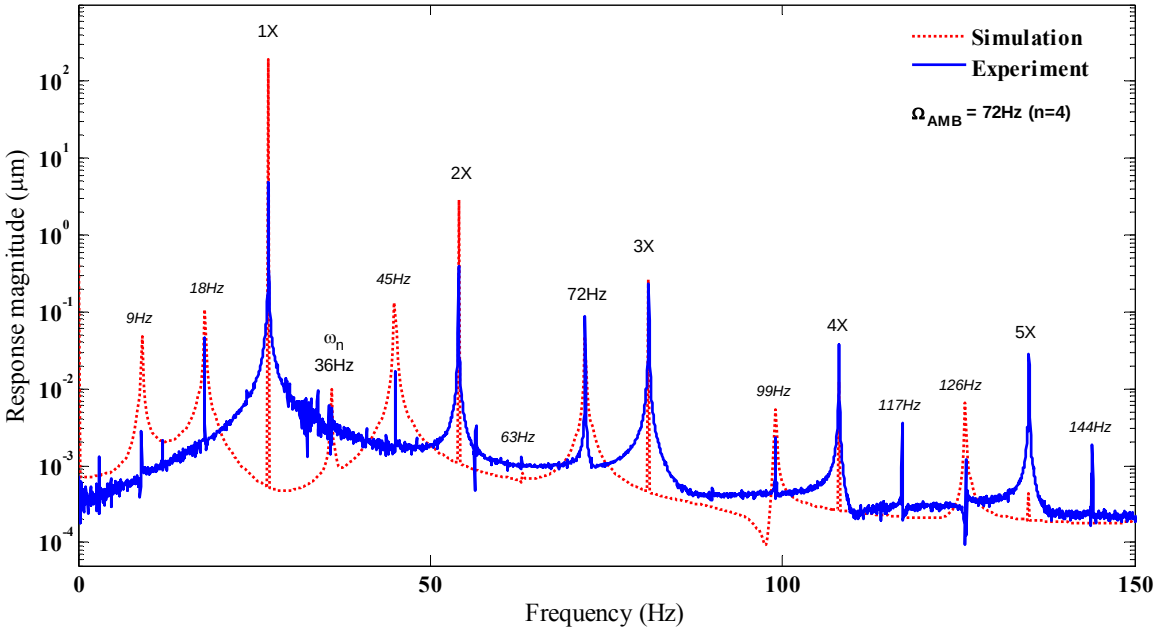

Figure 52 Comparison between simulation and experimental data, 40% cracked rotor. Ω=27 Hz and external force of 10 N.

CHAPTER VI

CONCLUSIONS

This research has investigated the application of an externally applied excitation force to the rotating rotor system for the purpose of shaft crack detection. The externally applied force of specific frequency and amplitude was generated by a magnetic actuator. This thesis has focused on the health monitoring, modeling, and analysis of rotating machines with breathing cracks, which open and close due to the self-weight of the rotor, producing a time-dependent stiffness leading to parametric excitation. Extensive experimental data has been collected, analyzed, and presented for comparison under different conditions. Simulations of a comparable finite element model have been presented in an effort to provide a robust condition monitoring and shaft crack diagnostic technique.

The experimental data of a healthy shaft shows that when AMB excitation is applied, small traces of combination frequencies sometimes appear which can be

considered negligible. However, when a crack is introduced to the shaft with AMB excitation, the presence of combination frequencies is clearly evident. Practically all calculated combination frequencies appear in the FFT spectrums for the cracked shafts. Further, as the depth of the shaft crack increases from 25% to 40%, the amplitudes of the combination frequencies increase, showing a clear growing trend. In addition, the system identification using an instrumented hammer showed that the cracked shaft exhibited a frequency shift for the third and fifth natural mode of the rotor.

The 25% and 40% cracked shafts with shims installed showed no significant difference in the FFT spectrum in comparison to the 25% and 40% un-shimmed cracked shafts. Shimming of the EDM cut was done in an attempt to more closely represent a real crack by filling in removed material with stainless steel. Magnified photos of the shim indicated that it fit well and left virtually no void. These results suggest that it may be reasonable to represent a crack with a simple notch in the shaft for experimental purposes.

Simulations using the finite element method produced results that closely resembled the equivalent experimental data. Essentially all calculated combination frequencies are present in the FFT plots as well as all other frequencies such as running speed and its multiples, AMB injection frequency, and the natural frequency. The simulations show that in the healthy shaft, no combination frequencies appear. However, when the crack is introduced, the combination frequencies are present and increase in amplitude with the increase in crack depth, similar to the experimental results.

Direct FFT plot comparisons of the experimental data and simulations are presented. This is done for the 40% cracked shaft with AMB excitations of n=2, n=3,

and n=4. These comparisons show that the frequency content of the simulations match the experimental data very well.

It has been demonstrated that simulated results correlate very well with comparable experimental data. The finite element technique used to calculate the response of the cracked shaft under AMB excitation can be applied to any rotor to calculate the rotor's combination frequencies. The presence of these frequencies on the FFT spectrum seems to indicate the existence of a shaft crack. Knowing the combination frequencies of a shaft excited by magnetic force actuator, one can potentially monitor the condition of a shaft online by examining the FFT spectrum for those frequencies. This rotor health monitoring technique would not require the shutdown of the machine and potentially reduce costly downtime and inspection processes.

BIBLIOGRAPHY

[1] J. Taylor, *The Vibration Analysis Handbook*. Vibration Consultants Inc, 2003.

[2] M. L. Adams, *Rotating Machinery Vibration*. New York: Marcel Dekker, Inc., 2000.

[3] R. B. McMillian, *Rotating Machinery: Practical Solutions to Unbalance and Misalignment*. Lilburn: THE FAIRMONT PRESS, INC., 2004.

[4] P. Girdhar, *Practical Machinery Vibration Analysis and Predictive Maintenance*. Burlington: Elsevier, 2004.

[5] A. Muszynska, *Rotordynamics*. CRC Press, 2005.

[6] S. Ganeriwala, S. Patel, and H. A. Hartung, "The Truth Behind Misalignment Vibration Spectra of Rotating Machinery".

[7] H. Ulbrich, "Comparison of Different actuator Concepts for Applications in Rotating Machinery," *International Journal of Rotating Machinery*, vol. 1, no. 1, pp. 61-71, 1994.

[8] P. G. Morton, "The derivation of bearing characteristics by means of transient excitation applied directly to a rotating shaft," *IUTAM Symposium, Dynamics of Rotors*, pp. 350-370, 1975.

[9] C. Won-Lee, "Mechatronics in Rotating Machinery," *7th IFToMM-Conference on Rotor Dynamics*, Sep. 2006.

[10] R. Nordmann and K. Schollhorn, "Identification of modal parameters of an elastic

rotor with oil film bearings," *ASME Journal of Vibration, Acoustics, Stress, and Reliability in Design*, vol. 106, 1984.

[11] J. Tonnesen and J. Lund, "Experimental techniques for rotordynamic analysis," *CISM Course No. 297, Rotordynamics 2*, 1988.

[12] T. Iwatsubo, S. Arii, and A. Oks, "Detection of a transverse crack in a rotor shaft by adding external force," *IMechE Vibrations in Rotating Machinery*, pp. C432/093275-282, 1992.

[13] J. T. Sawicki, M. I. Friswell, A. W. Wroblewski, and A. H. Pesch, "Condition Monitoring of Rotor Using Active Magnetic Actuator," *Proceedings of ASME Turbo Expo: Power for Land, Sea and Air*, Jun. 2008.

[14] R. A. Gasch, "Survey of the Dynamic Behavior of a Simple Rotating Shaft with a Transverse Crack," *Journal of Sound and Vibration*, no. 160, pp. 313-332, 1993.

[15] J. T. Sawicki, X. Wu, G. Y. Baaklini, and A. L. Gyekenyesi, "Vibration-Based Crack Diagnosis in Rotating Shafts During Acceleration through Resonance," *Proc. of SPIE 10th Annual International Symposium on Smart Structures and Materials*, 2003.

[16] J. T. Sawicki, A. L. Gyekenyesi, and G. Y. Baaklini, "Analysis of transient response of cracked flexible rotor," *SPIE's NDE and Health Monitoring of Aerospace Materials and Composites*, Mar. 2004.

[17] J. J. Sinou and A. W. Lees, "The Influence of Cracks in Rotating Shafts," *Journal of Sound and Vibration*, vol. 285, pp. 1015-1037, 2005.

[18] J. J. Sinou and A. W. Lees, "A Non-Linear Study of a Cracked Rotor," *European Journal of Mechanics A/Solids*, pp. 152-170, 2007.

[19] Y. Ishida and T. Inoue, "Detection of a Rotor Crack Using a Harmonic Excitation and Nonlinear Vibration Analysis," *Journal of Vibration and Acoustics*, vol. 128, p. 741, Dec. 2006.

[20] D. D. Quinn, et al., "Damage Detection of a Rotating Cracked Shaft Using an Active Magnetic Bearing as a Force Actuator -- Analysis and Experiment," *IEEE/ASME Transactions on Mechatronics*, vol. 10, no. 6, Dec. 2005.

[21] T. Bash, "Active Magnetic Bearings used as an Actuator for Rotor Health Monitoring in Conjunction with Conventional," *Master's Thesis, Department of Mechanical Engineering,Virginia Tech*, 2005.

[22] M. P. Cartmell, *Introduction to Linear, Parametric, and Nonlinear Vibrations*. London, UK: Chapman and Hall, 1990.

[23] D. W. Jordan and P. Smith, *Nonlinear Ordinary Differential Equations*. Oxford University Press, 1977.

[24] J. T. Sawicki, X. Wu, M. I. Friswell, and G. Y. Baaklini, "Finite Element Analysis of Coupled Lateral and Torsional Vibrations of a Rotor with Multiple Cracks," *Turbo Expo: Power for Land, Sea and Air*, Jun. 2005.

[25] M. I. Friswell, J. E. Penny, and C. Zhou, "Condition Monitoring of Rotating Machinery using Active Magnetic Bearings," *ISMA*, pp. 3497-3506, 2006.

[26] M. E. Kasarda, et al., "A Magnetic Bearing Actuator for Detection of Shaft Cracks

in Rotating Machinery Supported in Conventional Bearings," *Tenth International Symposium on Magnetic Bearings*, 2006.

[27] G. Mani, et al., "Damage Detection of a Rotating Cracked Shaft Using an Active Magnetic Bearing as a Force Actuator," *Ninth International Symposium on Magnetic Bearings*, Aug. 2004.

[28] Bently-Nevada. (2007, Oct.) General Electric Power . [Online]. http://www.gepower.com/prod_serv/products/oc/en/downloads/172179.pdf

[29] A. Technologies. (2003, Jan.) Agilent. [Online]. http://www.home.agilent.com/upload/cmc_upload/All/5966-3063.pdf

[30] J. S. Rao and R. Sreenivas, "Dynamics of Asymmetric Rotors using Solid Models," *IGTC 2003 Tokyo*, Nov. 2003.

[31] U. H. Hegazy, M. H. Eissa, and Y. A. Amer, "A Time-Varying Stiffness Rotor Active Magnetic Bearings Under Combined," *Journal of Applied Mechanics*, vol. 75, Jan. 2008.

[32] M. Karthikeyen, R. Tiwari, and S. Talukdar, "Development of a Novel Algorithm for a Crack Detection, Localization, and Sizing in a Beam Based on Forced Response Measures," *Journal of Vibration and Acoustics*, vol. 130, Apr. 2008.

[33] H. F. Castro, et al., "Experimental Performance Evaluation of Magnetic Actuator used in Rotating Machinery Analysis," *Journal of the Braz. Soc. of Mech. Sci. & Eng.*, vol. XXIX, no. 1, p. 99, Jan. 2007.

[34] M. Aenis and R. Nordmann, "Fault Diagnosis in a Centrifugal Pump using Active

Magnetic Bearings," *Ninth International Symposium on Transport Phenomena and Dynamics of Rotating Machinery*, Feb. 2002.

[35] G. M. Silva and R. Pederiva, "Fault Diagnosis in a Rotor Supported by Active Magnetic Bearings," *Seventh IFToMM-Conference on Rotor Dynamics*, Sep. 2006.

[36] I. S. Cade, P. S. Keogh, and M. N. Sahinkaya, "Fault Identification in Rotor Magnetic Bearing Systems Using Discrete Time Wavelet Coefficients," *Ninth International Symposium on Magnetic Bearings*, Aug. 2004.

[37] C. W. Lee, "Mechatronics in Rotating Machinery," *Seventh IFToMM-Conference on Rotor Dynamics*, pp. 25-28, Sep. 2006.

[38] P. N. Saavedra and L. A. Cuitino, "Vibration Analysis of Rotor for Crack Identification," *Journal of Vibration and Control*, vol. 8, pp. 51-67, 2002.

[39] D. E. Bently, C. T. Hatch, and B. Grissom, *Fundamentals of Rotating Machinery Diagnostics*. Minden, Nevada, USA: Bently Pressurized Bearing Press, 2002.

[40] D. Norfield, *Practical Balancing of Rotating Machinery*. Kidlington: Elsevier Ltd., 2006.

[41] D. N. Walker, *Torsional Vibration of Turbomachinery*. McGraw-Hill Professional, 2004.

[42] A. Muszynska, "Vibrational Diagnostics of Rotating Machinery Malfunctions," *International Journal of Rotating Machinery*, vol. 1, no. 3-4, pp. 237-266, 1995.

[43] L. Cheng, N. Li, X.-f. Chen, and Z.-j. He, "Discussion on the Dynamic Model of Cracked Rotor".

[44] J. T. Sawicki, G. Y. Baaklini, and A. L. Gyekenyesi, "Coupled Lateral and Torsional Vibrations of a Cracked Rotor," *Proceedings of ASME Turbo Expo*, Jun. 2004.

[45] J. T. Sawicki, X. Wu, A. L. Gyekenyesi, and G. Y. Baaklini, "Application of Nonlinear Dynamics Tools for Diagnosis of Cracked Rotor Vibration Signatures," *SPIE's Int. Symposium on Smart Structures and Materials*, 2005.

[46] J. T. Sawicki, "Some Advances in Diagnostics of Rotating Machinery Malfunctions," *Proceedings of the Int. Symposium on Machine Condition Monitoring and Diagnosis*, pp. 138-143, 2002.

APPENDICES

A. Supplemental Test Rig Images

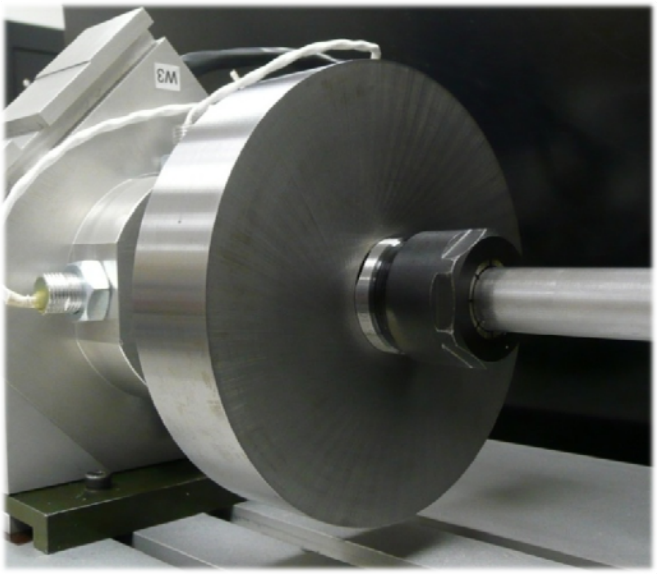

Figure A-1 5”×1” Disk.

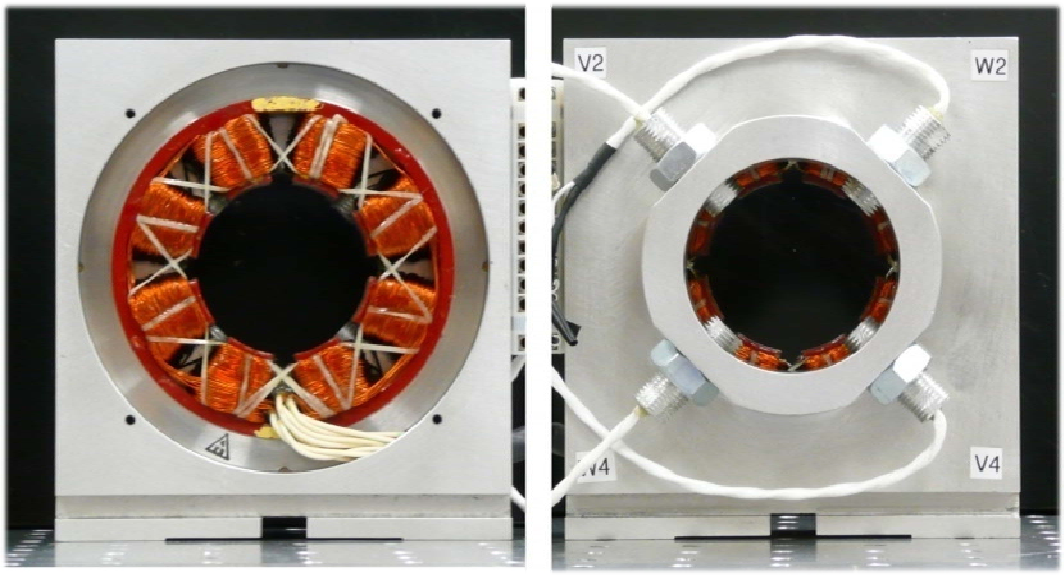

Figure A-2 AMB front and rear view.

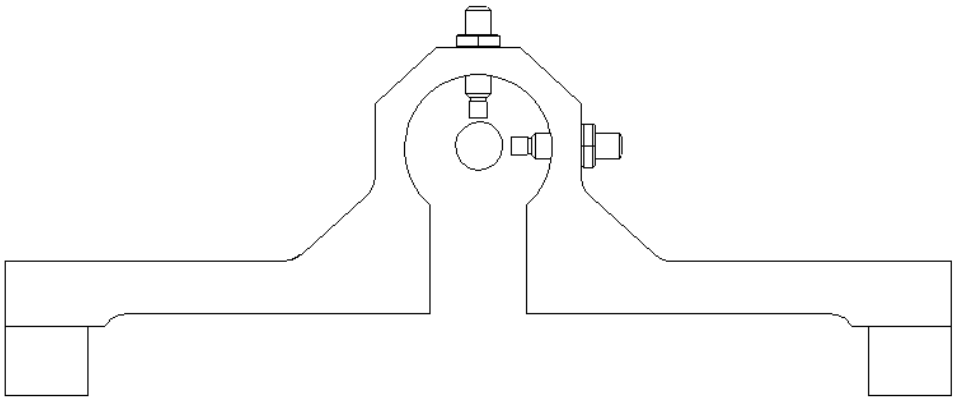

Figure A-3 Side view of Bently-Nevada® proximity probes mounting block.

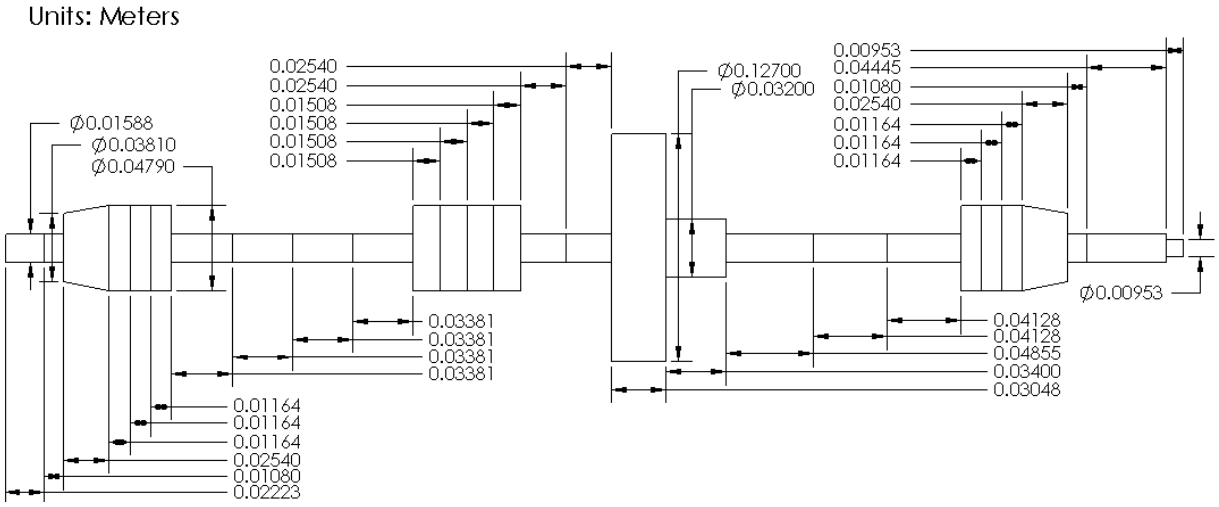

Figure A-4 Detailed FE model used in simulations.

B. Supplemental Data Acquisition System Images

Figure B-1 ADRE® 408DSPi data acquisition unit.

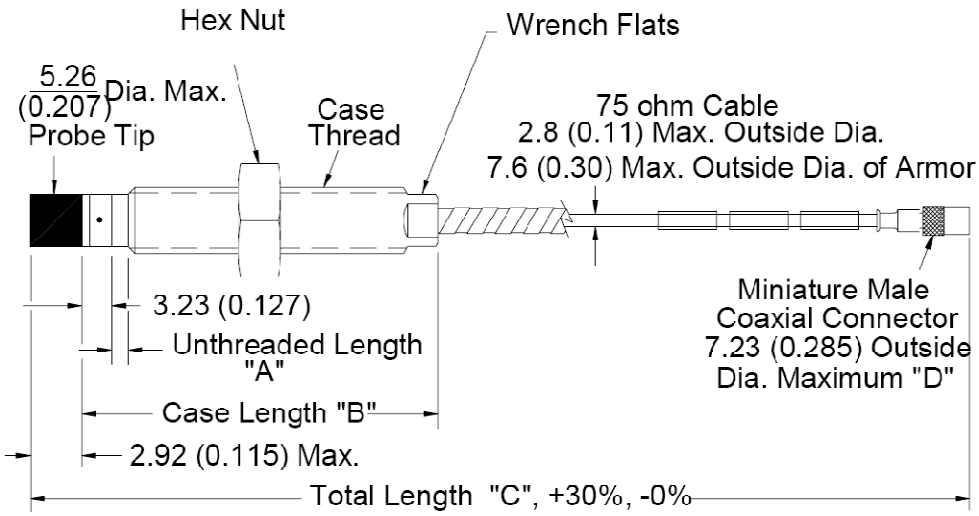

Figure B-2 3300 NSv proximity probes, standard mount.

Figure B-3 HP 35670A Dynamic Signal Analyzer.

C. Test Matrix

Trial	Test Type	Shaft Type	Signal Injection
1	Hammer (non-rotating)	Healthy	Hammer
2	No Signal Injection	Healthy	none
3	AMB Signal Injection	Healthy	n=2 (18Hz)
4	AMB Signal Injection	Healthy	n=3 (45Hz)
5	AMB Signal Injection	Healthy	n=4 (72Hz)
6	No Signal Injection	25% Un-shimmed Crack	none
7	AMB Signal Injection	25% Un-shimmed Crack	n=2 (18Hz)
8	AMB Signal Injection	25% Un-shimmed Crack	n=3 (45Hz)
9	AMB Signal Injection	25% Un-shimmed Crack	n=4 (72Hz)
10	Hammer (non-rotating)	40% Un-shimmed Crack	Hammer
11	No Signal Injection	40% Un-shimmed Crack	none
12	AMB Signal Injection	40% Un-shimmed Crack	n=2 (18Hz)
13	AMB Signal Injection	40% Un-shimmed Crack	n=3 (45Hz)
14	AMB Signal Injection	40% Un-shimmed Crack	n=4 (72Hz)
15	No Signal Injection	25% Shimmed Crack	none
16	AMB Signal Injection	25% Shimmed Crack	n=2 (18Hz)
17	AMB Signal Injection	25% Shimmed Crack	n=3 (45Hz)
18	AMB Signal Injection	25% Shimmed Crack	n=4 (72Hz)
19	No Signal Injection	40% Shimmed Crack	none
20	AMB Signal Injection	40% Shimmed Crack	n=2 (18Hz)
21	AMB Signal Injection	40% Shimmed Crack	n=3 (45Hz)
22	AMB Signal Injection	40% Shimmed Crack	n=4 (72Hz)

Table C-1 Complete experimental test matrix.